A Comparative Analysis of SARS-CoV-2 Antivirals Characterizes 3CL^pro Inhibitor PF-00835231 as a Potential New Treatment for COVID-19

Maren de Vries,[a] Adil S. Mohamed,[a] Rachel A. Prescott,[a,b] Ana M. Valero-Jimenez,[a] Ludovic Desvignes,[c,d] Rebecca O'Connor,[e] Claire Steppan,[e] Joseph C. Devlin,[b,f] Ellie Ivanova,[g] Alberto Herrera,[g] Austin Schinlever,[a,b] Paige Loose,[a] Kelly Ruggles,[f] Sergei B. Koralov,[g] Annaliesa S. Anderson,[h] Joseph Binder,[i] [ID] Meike Dittmann[a]

[a]Department of Microbiology, New York University Grossman School of Medicine, New York, New York, USA
[b]Vilcek Institute of Graduate Biomedical Sciences, New York University Grossman School of Medicine, New York, New York, USA
[c]Department of Medicine, New York University Grossman School of Medicine, New York, New York, USA
[d]Office of Science and Research, NYU Langone Health, New York, New York, USA
[e]Pfizer Discovery Sciences, Groton, Connecticut, USA
[f]Institute of Systems Genetics, New York University Grossman School of Medicine, New York, New York, USA
[g]Department of Pathology, New York University Grossman School of Medicine, New York, New York, USA
[h]Pfizer Vaccine Research and Development, Pearl River, New York, USA
[i]Pfizer Oncology Research and Development, San Diego, California, USA

ABSTRACT Severe acute respiratory syndrome coronavirus 2 (SARS-CoV-2) is the etiological agent of coronavirus disease 2019 (COVID-19). There is a dire need for novel effective antivirals to treat COVID-19, as the only approved direct-acting antiviral to date is remdesivir, targeting the viral polymerase complex. A potential alternate target in the viral life cycle is the main SARS-CoV-2 protease 3CL^pro (M^pro). The drug candidate PF-00835231 is the active compound of the first anti-3CL^pro regimen in clinical trials. Here, we perform a comparative analysis of PF-00835231, the preclinical 3CL^pro inhibitor GC-376, and the polymerase inhibitor remdesivir, in alveolar basal epithelial cells modified to express ACE2 (A549^+ACE2 cells). We find PF-00835231 with at least similar or higher potency than remdesivir or GC-376. A time-of-drug-addition approach delineates the timing of early SARS-CoV-2 life cycle steps in A549^+ACE2 cells and validates PF-00835231's early time of action. In a model of the human polarized airway epithelium, both PF-00835231 and remdesivir potently inhibit SARS-CoV-2 at low micromolar concentrations. Finally, we show that the efflux transporter P-glycoprotein, which was previously suggested to diminish PF-00835231's efficacy based on experiments in monkey kidney Vero E6 cells, does not negatively impact PF-00835231 efficacy in either A549^+ACE2 cells or human polarized airway epithelial cultures. Thus, our study provides *in vitro* evidence for the potential of PF-00835231 as an effective SARS-CoV-2 antiviral and addresses concerns that emerged based on prior studies in nonhuman *in vitro* models.

IMPORTANCE The arsenal of SARS-CoV-2 specific antiviral drugs is extremely limited. Only one direct-acting antiviral drug is currently approved, the viral polymerase inhibitor remdesivir, and it has limited efficacy. Thus, there is a substantial need to develop additional antiviral compounds with minimal side effects and alternate viral targets. One such alternate target is its main protease, 3CL^pro (M^pro), an essential component of the SARS-CoV-2 life cycle processing the viral polyprotein into the components of the viral polymerase complex. In this study, we characterize a novel antiviral drug, PF-00835231, which is the active component of the first-in-class 3CL^pro-targeting regimen in clinical trials. Using 3D *in vitro* models of the human airway epithelium, we demonstrate the antiviral potential of PF-00835231 for inhibition of SARS-CoV-2.

Address correspondence to Meike Dittmann, Meike.Dittmann@nyulangone.org.

In December 2019, multiple cases of severe pneumonia with unexplained etiology were reported in Wuhan, China (1). The infectious agent was identified as a novel member of the family *Coronaviridae* (1), later named severe acute respiratory syndrome coronavirus 2 (SARS-CoV-2) (2). The resulting disease, coronavirus disease 2019 (COVID-19), has since become a deadly pandemic.

A number of candidate drugs that may inhibit SARS-CoV-2 infection and replication have been proposed. However, only one direct-acting antiviral is currently approved for the treatment of COVID-19, namely remdesivir, a nucleoside analog that inhibits the SARS-CoV-2 RNA-dependent RNA-polymerase (RdRp). Remdesivir is incorporated into viral RNA by the RdRp, resulting in chain termination of both viral transcripts and *de novo* synthesized viral genomes (3). Given this considerably limited arsenal of direct-acting antivirals for COVID-19, it remains a strategic priority to develop novel compounds with minimal side effects and that are directed against alternate viral targets.

One such alternate SARS-CoV-2 target is its main protease, 3CL^{pro} (M^{pro}), which plays an essential role in the viral life cycle. Upon entry and uncoating of the viral particles, the positive-stranded RNA genome is rapidly translated into two polyproteins which are subsequently processed into functional proteins by PL2^{pro} and 3CL^{pro} viral proteases (4). 3CL^{pro} is the main protease and is responsible for releasing 11 of the 13 individual proteins, including the polymerase subunits, enabling their proper folding and assembly into the active polymerase complex (5). Thus, blocking 3CL^{pro} activity effectively shuts down the life cycle before viral transcription or replication occur, making it an enticing target for intervention (6). In addition, 3CL^{pro} has a unique substrate preference (Leu-Gln ↓ {Ser, Ala, Gly}), a preference not shared by any known human protease, implying the potential for high selectivity and low side effects of 3CL^{pro}-targeting drugs (7). Although there have been intense efforts to develop 3CL^{pro} inhibitors specific for SARS-CoV-2 (6–13), only one inhibitor has been brought to the clinic, PF-07304814, which is the first anti-3CL^{pro} compound in clinical trials.

PF-07304814 is a ketone-based covalent cysteine protease inhibitor (9). It is administered as a phosphate prodrug, which is then metabolized to its active form, PF-00835231 (14). PF-00835231 was initially designed in response to a previous coronavirus epidemic in 2003, as an inhibitor for the 3CL^{pro} of SARS-CoV (9). However, with SARS-CoV disease declining, clinical studies were not practical and, consequently, PF-00835231 was never tested in patients. Because 3CL^{pro} of SARS-CoV and SARS-CoV-2 are 96% identical at the amino acid level, including 100% identity within the catalytic pocket (7), it seemed reasonable to assume that PF-00835231 may inhibit SARS-CoV-2 as well.

Indeed, a recent study demonstrated antiviral activity of PF-00835231 against SARS-CoV-2, albeit at high micromolar levels (14). The study was performed in Vero E6 cells, a monkey kidney cell line in which SARS-CoV-2 replicates to high titers, but which is known to express high levels of the efflux transporter P-glycoprotein (also known as multidrug resistance protein 1 [MDR1] and encoded by gene ATP binding cassette subfamily B member 1, *ABCB1*) (15). Inhibiting MDR1 function significantly increased antiviral efficacy in Vero E6 cells, suggesting that PF-00835231 is an MDR1 substrate (14). MDR1 is well studied in the context of human immunodeficiency virus 1 (HIV-1) protease inhibitors such as lopinavir or ritonavir, where it reduces intracellular protease inhibitor levels and contributes to drug resistance in T cells and monocytes (16). In contrast to HIV-1, where viral replication is essentially limited to T cells and monocytes, SARS-CoV-2 infects multiple organs and cell types throughout the human body, with the first and major site of replication being cells of the respiratory tract (17, 18). Thus, to investigate the potential role of MDR1 on antiviral potency of PF-00835231 against SARS-CoV-2, it is imperative to utilize experimental model systems representing the human airways.

Here, we characterize the antiviral potency and cytotoxicity profile of PF-00835231 in two human airway models, a human type II alveolar epithelial cell line and polarized human airway epithelial cultures. In side-by-side experiments, we place PF-00835231's antiviral efficacy against SARS-CoV-2 in the context of another, preclinical 3CL^pro inhibitor, GC-376, and of the current standard of care, remdesivir. Finally, we address the impact of P-glycoprotein (MDR1) on PF-00835231's antiviral efficacy in the human airways.

RESULTS

Establishing A549^{+ACE2} cells as a tool to determine SARS-CoV-2 infection and cytopathic effect by high-content microscopy. The human adenocarcinoma alveolar epithelial cell line A549 is a workhorse cell line in the study of respiratory viruses. However, A549 cells are not permissive to SARS-CoV-2 infection, as they do not highly express the SARS-CoV-2 receptor ACE2 (19). To make A549 cells amenable for experiments with SARS-CoV-2, we generated a stable A549 cell line expressing ACE2 exogenously. We confirmed elevated levels of ACE2 mRNA in A549^{+ACE2} cells by reverse transcription-quantitative PCR (RT-qPCR), and of ACE2 protein by Western blotting, flow cytometry, and confocal microscopy (Fig. 1a to e).

To determine permissiveness, we infected A549 or A549^{+ACE2} cells with a serial dilution of SARS-CoV-2, in a 96-well format, for 24 h. Using immunofluorescence staining for SARS-CoV-2 nucleocapsid protein (N) and high-content microscopy, we found A549^{+ACE2} cells permissive to SARS-CoV-2 infection, whereas parent A549 cells were not (Fig. 1f).

Since the discovery of SARS-CoV-2, limited evolution has been observed, which has been attributed to the proofreading mechanism of coronavirus polymerases (20). The two major lineages of SARS-CoV-2 circulating globally as of time of writing are represented by the Wuhan basal clade and the spike protein D614G clade, also referred to as clades A and B, respectively (21). Compared to clade A, clade B isolates carry a mutation in the spike-encoding gene S, which results in the amino acid substitution D614G. D614G is frequently accompanied by an additional mutation in open reading frame 1b (ORF1b), which encodes the RNA-dependent RNA-polymerase complex (RdRp), resulting in substitution P323L in the polymerase subunit NSP12 (22). Clade B viruses are more prevalent globally, which might be due to their increased efficiency infecting cells in the upper respiratory tract and subsequently increased transmissibility, enabled by the spike D614G mutation (23, 24).

To characterize the viral growth of representatives from the two major clades in our model, we challenged A549^{+ACE2} cells with the clinical SARS-CoV-2 isolate USA-WA1/2020, a clade A representative (25), or with USA/NYU-VC-003/2020, a clade B representative, the latter of which we had isolated in March 2020 (26). USA/NYU-VC-003/2020 carries both of the signature clade B amino acid changes, S D614G and NSP12 P323L, but its 3CL^pro sequence is identical to that of USA-WA1/2020. In low multiplicity of infection (MOI) growth kinetics on A549^{+ACE2} cells, we found that the growth of clade B USA/NYU-VC-003/2020 exceeds that of clade A USA-WA1/2020, especially at later times of infection (Fig. 1g). We were able to detect *de novo* produced infectious particles as soon as 12 h postinfection (hpi) for USA-WA1/2020, suggesting that the SARS-CoV-2 life cycle in A549^{+ACE2} cells is completed by that time. In terms of producing infectious titers, USA/NYU-VC-003/2020 initially lagged behind USA-WA1/2020, but then yielded significantly higher titers at 48 and 72 hpi.

Finally, we observed that the cytopathic effect (CPE) caused by SARS-CoV-2 on A549^{+ACE2} cells manifests in syncytium formation, in which the nuclei form a ring-like structure (Fig. 1h). This effect had previously been described for other coronaviruses (27, 28), although the exact mechanism for the ring-like nuclear structure formation remains to be elucidated. Together, our data establish A549^{+ACE2} cells as a tractable tool to study SARS-CoV-2 infection, spread, and cytopathic effect.
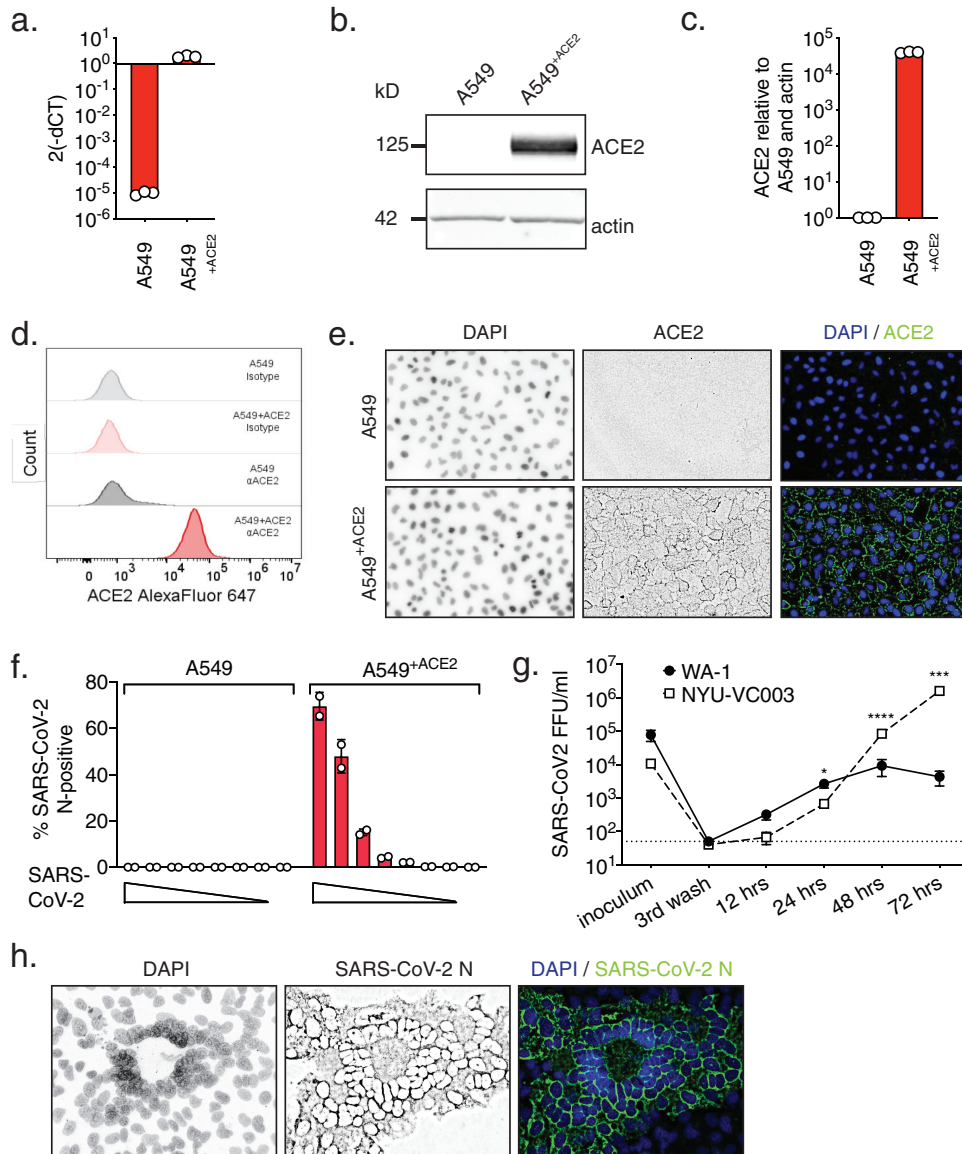
FIG 1 Validation of A549[+ACE2] cells as a tool to study SARS-CoV-2. A549[+ACE2] cells were generated by lentiviral transduction delivering an ACE2 overexpression construct and subsequent bulk-selection. (a to e) ACE2 expression in A549 parental or A549[+ACE2] cells determined by reverse transcription-quantitative PCR (RT-qPCR) (a); Western blot (b and c), quantified in panel c; flow cytometry (d); or microscopy (e). (f) A549 parental or A549[+ACE2] cells were infected with a serial dilution of SARS-CoV-2 USA-WA1/2020. At 24 h, cells were fixed and stained for SARS-CoV-2 N protein, and infected cells were quantified by high-content microscopy. Mean ± standard error of the mean (SEM) from duplicate wells. (g) A549[+ACE2] cells were infected with SARS-CoV-2 USA-WA1/2020 or USA/NYU-VC-003/2020 at a multiplicity of infection (MOI) of 0.01, and infectious progeny titers, collected from supernatants over time, determined by focus-forming assay on A549[+ACE2] cells. Mean ± SEM from $n = 3$ independent experiments. Unpaired t test; *, $P < 0.05$; ***, $P < 0.001$; ****, $P < 0.0001$. (h) Confocal microscopy of SARS-CoV-2 syncytia in A549[+ACE2] cells at 48 hpi.

PF-00835231 potently inhibits SARS-CoV-2 in A549[+ACE2] cells. PF-00835231 is the active compound of the first anti 3CL[pro] regimen currently tested in clinical trials (9). We studied and compared three compounds in regard to SARS-CoV-2 antiviral activity and cytotoxicity, as follows: (i) PF-00835231, (ii) the preclinical 3CL[pro] inhibitor GC-376, which is licensed for veterinary use in feline coronavirus infections (29) and was recently shown to inhibit SARS-CoV-2 in Vero E6 cells (30), and (iii) the polymerase inhibitor remdesivir, which is currently the only direct-acting antiviral approved in the United States to treat SARS-CoV-2 infections, and is thus the standard of care. We
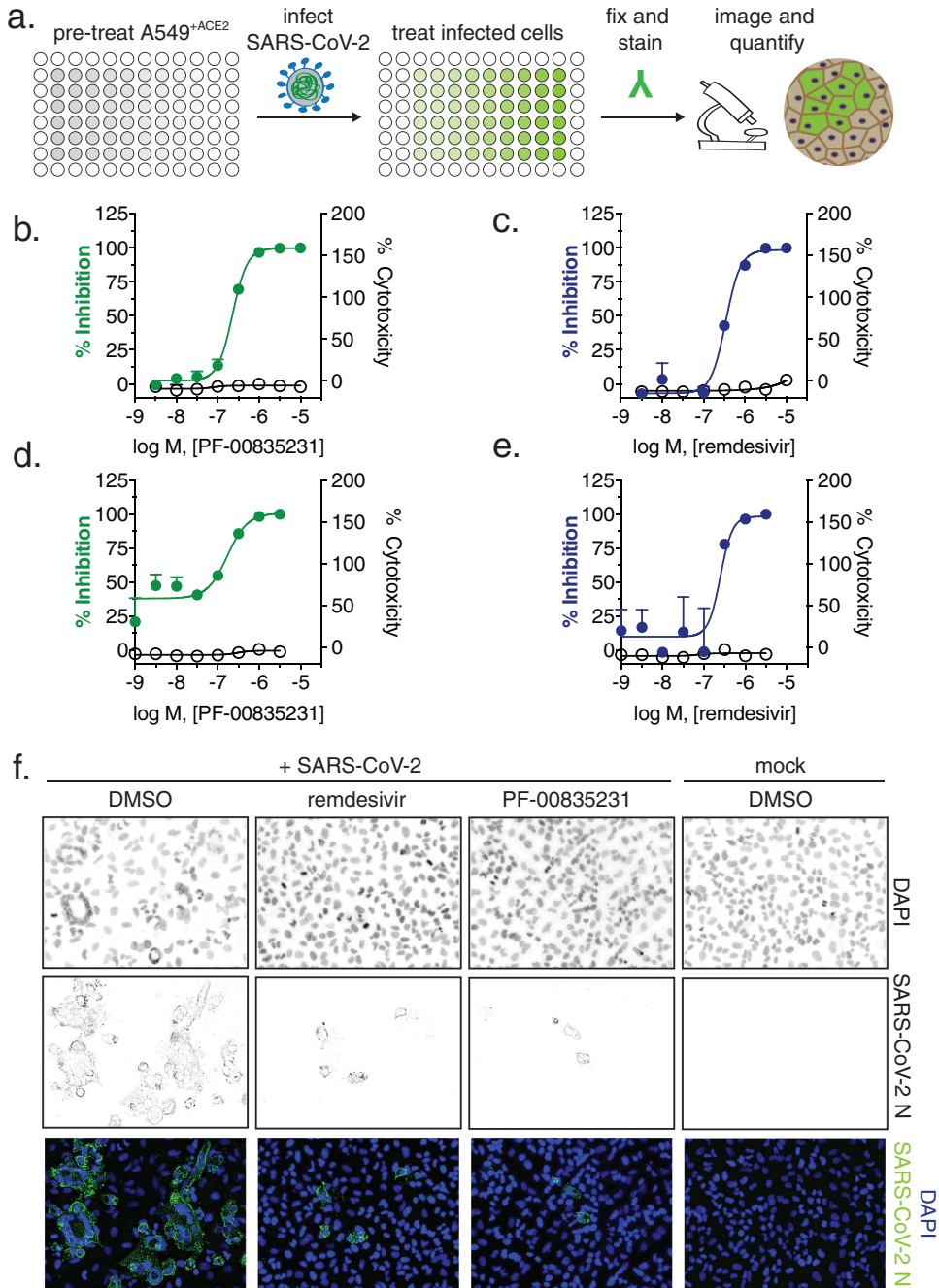
FIG 2 Antiviral SARS-CoV-2 activity and cytotoxicity of PF-00835231, and remdesivir in A549^{+ACE2} cells. (a) Antiviral assay workflow. A549^{+ACE2} cells were pretreated with serial dilutions of PF-00835231 or remdesivir, then infected with SARS-CoV-2 while continuing drug treatment. At 24 or 48 h, cells were fixed and stained for SARS-CoV-2 N protein, and infected cells were quantified by high-content microscopy. Cytotoxicity was measured in similarly treated but uninfected cultures via CellTiter-Glo assay. Values for 50% effective concentration (EC$_{50}$), EC$_{90}$, and 50% cytotoxic concentration (CC$_{50}$) from $n = 3$ independent experiments are listed in Table 1. (b) PF-00835231, and (c) remdesivir antiviral activity and cytotoxicity in A549^{+ACE2} cells infected with SARS-CoV-2 USA-WA1/2020 for 24 h. Representative graphs are shown. (d) PF-00835231, and (e) remdesivir antiviral activity and cytotoxicity in A549^{+ACE2} cells infected with SARS-CoV-2 USA/NYU-VC-003/2020 for 24 h. Representative graphs are shown. (f) Representative images of SARS-CoV-2 USA-WA1/2020 syncytium formation at 48 hpi in A549^{+ACE2} cells under treatment with 0.33 μM PF-00835231 or remdesivir.

exposed A549^{+ACE2} cells with escalating doses of the three respective drugs, challenged them with SARS-CoV-2, and measured virus antigen (N)-expressing cells by high-content microscopy (Fig. 2a). In parallel, we determined cellular viability by measuring ATP levels in drug-treated but uninfected cells. Antiviral assays were performed with both our clade A and clade B SARS-CoV-2 representatives.

TABLE 1 Antiviral efficacy and cytotoxicity of PF-00835231 versus remdesivir on A549^{+ACE2} cells

Strain or drug	Time (hpi)	EC$_{50}$ (μM)	95% CI[c]	P value Drug vs drug[a]	P value Isolate vs isolate[b]	EC$_{90}$ (μM)	95% CI	CC$_{50}$ (μM)[d]
USA-WA1/2020								
PF-00835231	24	0.221	0.137–0.356			0.734	0.391–1.38	>10
	48	0.158	0.0795–0.314			0.439	0.380–0.508	>10
Remdesivir	24	0.442	0.240–0.814	0.002		1.19	0.622–2.28	>10
	48	0.238	0.122–0.436	0.035		0.529	0.534–0.656	>10
USA/NYU-VC-003/2020								
PF-00835231	24	0.184	0.016–0.377		0.307	0.591	0.534–0.654	>10
Remdesivir	24	0.238	0.200–0.400	0.028	0.024	0.589	0.416–0.834	>10

[a]50% effective concentration (EC$_{50}$) of remdesivir versus EC$_{50}$ of PF-00835231.
[b]EC$_{50}$ of drug versus EC$_{50}$ of the same drug for USA-WA1/2020.
[c]CI, confidence interval.
[d]CC$_{50}$, 50% cytotoxic concentration.

In a first set of experiments, we compared antiviral efficacy between PF-00835231 and remdesivir side by side (Fig. 2 and Table 1). PF-00835231 inhibited the clade A representative SARS-CoV-2 USA-WA1/2020 with average 50% effective concentrations (EC$_{50}$) of 0.221 μM at 24 h and 0.158 μM at 48 h (Fig. 2b and Table 1). As such, PF-00835231 was statistically more potent than remdesivir, with EC$_{50}$ values of 0.442 μM at 24 h and 0.238 μM at 48 h (Fig. 2c and Table 1). None of the compounds showed detectable cytotoxicity (Fig. 2b to e and Table 1). We then compared the antiviral efficacy of PF-00835231 and remdesivir for clade B USA/NYU-VC-003/2020. Due to cytopathic effects driven by USA/NYU-VC-003/2020 at the 48-h time point, we only determined antiviral efficacy at 24 h. PF-00835231 was inhibitory with an EC$_{50}$ of 0.184 μM, and was thus again statistically more potent than remdesivir (EC$_{50}$ = 0.283 μM).

Interestingly, only the polymerase inhibitor remdesivir exhibited statistically significantly weaker antiviral activity against the clade A isolate compared to the clade B isolate, with an EC$_{50}$ of 0.442 μM (versus clade A) and an EC$_{50}$ of 0.238 μM (versus clade B; Table 1). This might be an impact of the polymerase subunit NSP12 P323L mutation present in the clade B representative. Next, we analyzed microscopy data for drug-mediated inhibition of the CPE, including ring-shaped syncytium formation. PF-00835231 and remdesivir both decreased the overall number of infected foci and fully protected A549^{+ACE2} cells from ring syncytium formation at 0.33 μM and above (Fig. 2f and data not shown).

In a second set of experiments, we compared antiviral efficacy between PF-00835231 and GC-376 side by side (Fig. 3a to d and Table 2). PF-00835231 inhibited the clade A representative SARS-CoV-2 USA-WA1/2020 with EC$_{50}$ values of 0.422 μM at 24 h and 0.344 μM at 48 h (Fig. 3b and Table 2). This slight shift in EC$_{50}$ values compared to those in Table 1 can be explained by intra-assay variation, which is higher for live cell assays than it is for binding assays. For this reason, we could not compare PF-00835231 across assays. In the direct comparison, PF-00835231 trended toward being more potent than GC-376, which exhibited EC$_{50}$ values of 0.632 μM at 24 h and 0.696 μM at 48 h (Fig. 3b and Table 2). For clade B USA/NYU-VC-003/2020, PF-00835231 was inhibitory with an EC$_{50}$ of 0.326 μM, and thus again trended toward being more potent than GC-376 (EC$_{50}$ = 0.529 μM) (Fig. 3c and d and Table 2).

Both protease inhibitors, PF-00835231 and GC-376, had similar antiviral activities between the two clades in this assay (Tables 1 and 2). This is in line with the fact that 3CL^{pro} is identical in these two viruses. Finally, GC-376 decreased the number and size of viral foci, but was unable to protect cells from virus-induced CPE at 1 μM (Fig. 3e). In contrast, at 1 μM and above, PF-00835231 fully protected A549^{+ACE2} cells from CPE (Fig. 3e and data not shown).

Collectively, we show that, in this assay, PF-00835231 inhibits isolates from both major SARS-CoV-2 lineages at similar or better effective concentrations than remdesivir and the preclinical 3CL^{pro} inhibitor GC-376.
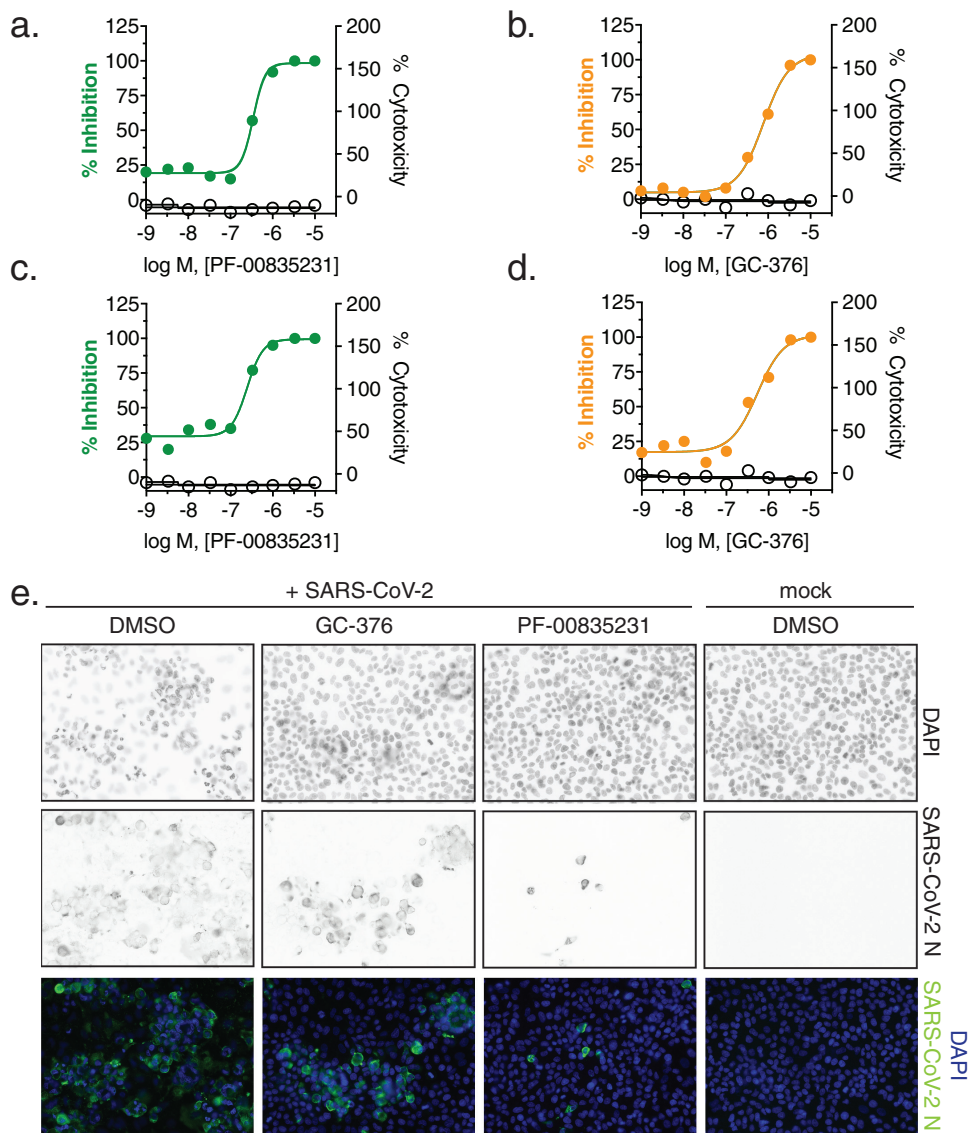
FIG 3 Antiviral SARS-CoV-2 activity and cytotoxicity of PF-00835231 and GC-376 in A549^{+ACE2} cells. Antiviral assay workflow as described in Fig. 2a. (a) PF-00835231 and (b) GC-376 antiviral activity and cytotoxicity in A549^{+ACE2} cells infected with SARS-CoV-2 USA-WA1/2020 for 24 h. Representative graphs are shown. (c) PF-00835231 and (d) GC-376 antiviral activity and cytotoxicity in A549^{+ACE2} cells infected with SARS-CoV-2 USA/NYU-VC-003/2020 for 24 h. Representative graphs are shown. (e) Representative images of SARS-CoV-2 USA-WA1/2020 syncytium formation at 48 hpi in A549^{+ACE2} cells under treatment with 1 μM PF-00835231 or GC-376.

Timing of PF-00835231 antiviral action against USA-WA1/2020 in A549^{+ACE2} cells is consistent with PF-00835231's role as a 3CL^{pro} inhibitor. PF-00835231 and remdesivir target different SARS-CoV-2 proteins (9, 31). PF-00835231 targets 3CL^{pro}, blocking polyprotein processing and thus formation of the viral polymerase complex (32). Remdesivir acts on the subsequent step, which is the incorporation of nucleotides into nascent viral RNA transcripts and genomes by the viral polymerase complex (3, 33).

To determine whether the action of PF-00835231 is consistent with its established role as a 3CL^{pro} inhibitor, and to delineate the timing of early SARS-CoV-2 life cycle stages in A549^{+ACE2} cells, we performed time-of-drug-addition experiments (34). This approach determines how long the addition of a drug can be delayed before it loses antiviral activity. Using 1-h-increments (from 1 h prior to 4 h postinfection), we varied the time of drug addition for a monoclonal neutralizing antibody (NAb) (viral

TABLE 2 Antiviral efficacy and cytotoxicity of PF-00835231 versus GC-376 on A549^{+ACE2} cells

Strain or drug	Time (hpi)	EC$_{50}$ (μM)	95% CI	P value for: Drug vs drug[a]	Isolate vs isolate[b]	EC$_{90}$ (μM)	95% CI	CC$_{50}$ (μM)
USA-WA1/2020								
PF-00835231	24	0.422	0.0836–2.13			0.978	0.326–2.93	>10
	48	0.344	0.0842–1.404			1.158	0.358–3.74	>10
GC-376	24	0.623	0.257–1.506	0.366		4.55	1.89–10.91	>10
	48	0.696	0.198–2.44	0.114		5.25	2.53–10.875	>10
USA/NYU-VC-003/2020								
PF-00835231	24	0.326	0.098–1.08		0.543	1.17	0.115–11.89	>10
GC-376	24	0.529	0.184–1.512	0.265	0.700	2.734	0.897–8.33	>10

[a]EC$_{50}$ of GC-376 versus EC$_{50}$ of PF-00835231.
[b]EC$_{50}$ of drug versus EC$_{50}$ of the same drug for USA-WA1/2020.

attachment inhibition control), GC-376 (3CL^{pro} inhibition control), PF-00835231, and remdesivir (RdRp inhibition control). We measured the percentage of SARS-CoV-2-infected cells via high-content microscopy at 12 hpi, which corresponds to one replication cycle in A549^{+ACE2} cells, as determined previously (Fig. 1g). We synchronized infection using a preincubation step at 4°C, followed by a transition to 37°C at 1 h post addition of virus, and used the minimum treatment doses for each drug that led to undetectable infection levels—3 μM for PF-00835231 and the neutralizing antibody and 10 μM for remdesivir and GC-376.

The neutralizing antibody lost its antiviral function first, starting at the first addition point postinfection (1 h), confirming blockage of attachment and entry as the mode of antiviral action (Fig. 4a). Interestingly, all three drugs, GC-376, PF-00835231, and remdesivir, lost antiviral action at the same time of addition, starting at 2 hpi, and with subsequently enhanced loss of activity at 3 and 4 hpi (Fig. 4a). This suggests that polyprotein processing and the start of viral transcription/translation follow each other very closely in time. These time-of-drug-addition experiments confirm the timing of PF-00835231's antiviral action during the early stages of intracellular virus propagation, consistent with its role as a 3CL^{pro} inhibitor. Furthermore, these experiments delineate the timing of the SARS-CoV-2 life cycle events in the tissue culture model of A549^{+ACE2} cells (Fig. 4b) and demonstrate that polymerase and protease inhibitors such as PF-00835231 can effectively block SARS-CoV-2 replication in cells when administered within a few hours after infection.

PF-00835231 is well-tolerated in polarized human airway epithelial cultures. The human respiratory tract is a major entry portal for viruses, including SARS-CoV-2,
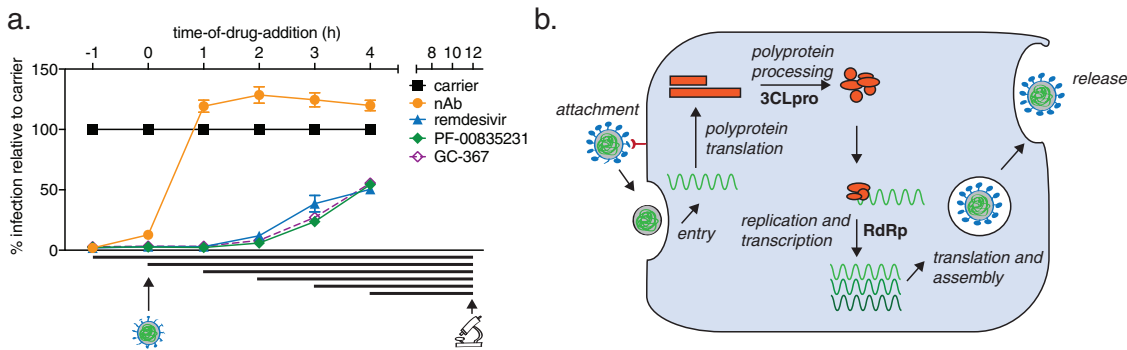
FIG 4 Time-of-drug-addition assay for PF-00835231, GC-376, remdesivir, and a neutralizing antibody in A549^{+ACE2} cells. (a) At the indicated time points, A549^{+ACE2} cells were infected with SARS-CoV-2 USA-WA1/2020, treated with 3 μM monoclonal neutralizing antibody (control for targeting attachment and entry), 10 μM the drug GC-376 (control drug for 3CL^{pro} inhibition), 3 μM PF-00835231 (3CL^{pro} inhibitor), or 10 μM remdesivir (RdRp inhibitor). At 12 h (one round of replication) cells were fixed and stained for SARS-CoV-2 N protein, and infected cells were quantified by high-content microscopy. Means $\pm$ SEM from $n = 3$ independent experiments. (b) Schematic of SARS-CoV-2 life cycle in A549^{+ACE2} cells. 3CL^{pro}, 3C-like protease; RdRp, RNA-dependent RNA polymerase.

and the first battle between host and virus occurs in cells of the respiratory epithelium. This specialized tissue contains three major cell types (basal, secretory, and ciliated) which are organized in a characteristic polarized architecture (35). As shown, human adenocarcinoma alveolar epithelial A549^{+ACE2} cells are permissive for SARS-CoV-2 infection and allow for high-throughput experiments (Fig. 1 and 4). However, they do not recapitulate the complexity and architecture of the human airway epithelium.

To test PF-00835231 and remdesivir in an additional, more physiologically relevant, yet lower-throughput human model system, we generated polarized human airway epithelial cultures (HAEC). HAEC contain multiple cell types of the airway epithelium and recapitulate its typical architecture (Fig. 5a to d), which makes HAEC arguably one of the most physiologically relevant models for *in vitro* studies of human respiratory pathogens. HAEC are permissive to SARS-CoV-2 infections and were utilized to obtain the very first SARS-CoV-2 isolate in December 2019 (1).

First, we performed in-depth analyses of the cellular heterogeneity of our HAEC model system by single-cell RNA sequencing (sc-RNAseq; Fig. 5b) (36). Gene expression profiling enabled resolution of distinct clusters with cell types assigned based on previously published transcriptional signatures (37, 38). We identified 7 different clusters as cycling basal, basal, suprabasal, secretory, ciliated, and microfold cells, as well as cells undergoing epithelial-mesenchymal transition (EMT; Fig. 5b). The EMT process in HAEC has previously been associated with loss of polarized organization as a consequence of remodeling (39) and is likely to occur at a low level at steady state in HAEC. Recapitulation of the major cell types and physiological conditions of the lung epithelium provided molecular confirmation for the HAEC system in assessing SARS-CoV-2 infection.

To establish the use of PF-00835231 in HAEC, we determined its cytotoxicity profile and compared it to that of remdesivir. We added PF-00835231 or remdesivir to the basolateral chamber of HAEC (Fig. 5a) and determined tissue morphology by histology and integrity of the epithelial layer by measuring transepithelial resistance (TEER; Fig. 5c to e). Neither drug caused measurable adverse effects on the morphology of the cultures (Fig. 5c and d). However, while remdesivir negatively impacted TEER over time, albeit not statistically significantly compared to untreated cultures, we did not observe this trend for PF-00835231 (Fig. 5e).

To complement our assessment of how well human epithelium tolerates these inhibitors, we took advantage of an alternative cytotoxicity assay on BCi-NS1.1 cells, the basal-like undifferentiated precursor cell monolayers used for generation of HAEC. We treated these monolayers with a dose range of PF-00835231 or remdesivir for 48 h, and quantified ATP as a measure of cell viability, similar to previous experiments with A549^{+ACE2} cells. We did not detect a decrease in ATP upon PF-00835231 treatment, even at the largest amount of drug (10 μM) tested. In contrast, 10 μM remdesivir caused a reduction in ATP levels compared to carrier control, albeit not statistically significantly (Fig. 5f). These experiments demonstrate that both drugs are well-tolerated in our model of polarized human airway epithelium.

PF-00835231 exhibits potent anti-SARS-CoV-2 activity in HAEC. To determine PF-00835231's anti-SARS-CoV-2 activity in HAEC, we added either 0.025, 0.5, or 10 μM PF-00835231 or remdesivir, or dimethyl sulfoxide (DMSO) carrier control, to the basolateral chamber of HAEC (Fig. 6a to c). We then challenged HAEC apically with SARS-CoV-2 USA-WA1/2020, and determined viral infectious titers from apical washes collected at 12-h increments.

We first detected progeny viral particles in apical washes from DMSO-treated cultures at 12 hpi (Fig. 6a and b), indicating that the SARS-CoV-2 life cycle in HAEC cells is completed by that time. Both PF-00835231 and remdesivir potently inhibited SARS-CoV-2 titers in a dose-dependent manner, with the 10 μM doses resulting in viral titers below the limit of detection at most time points (Fig. 6a and b).

To visualize SARS-CoV-2 infection in HAEC during drug treatment, we fixed infected HAEC at the 72-h endpoint and stained them for SARS-CoV-2-N-expressing cells (Fig. 6c). In carrier control cultures, we observed robust infection. Upon treatment with
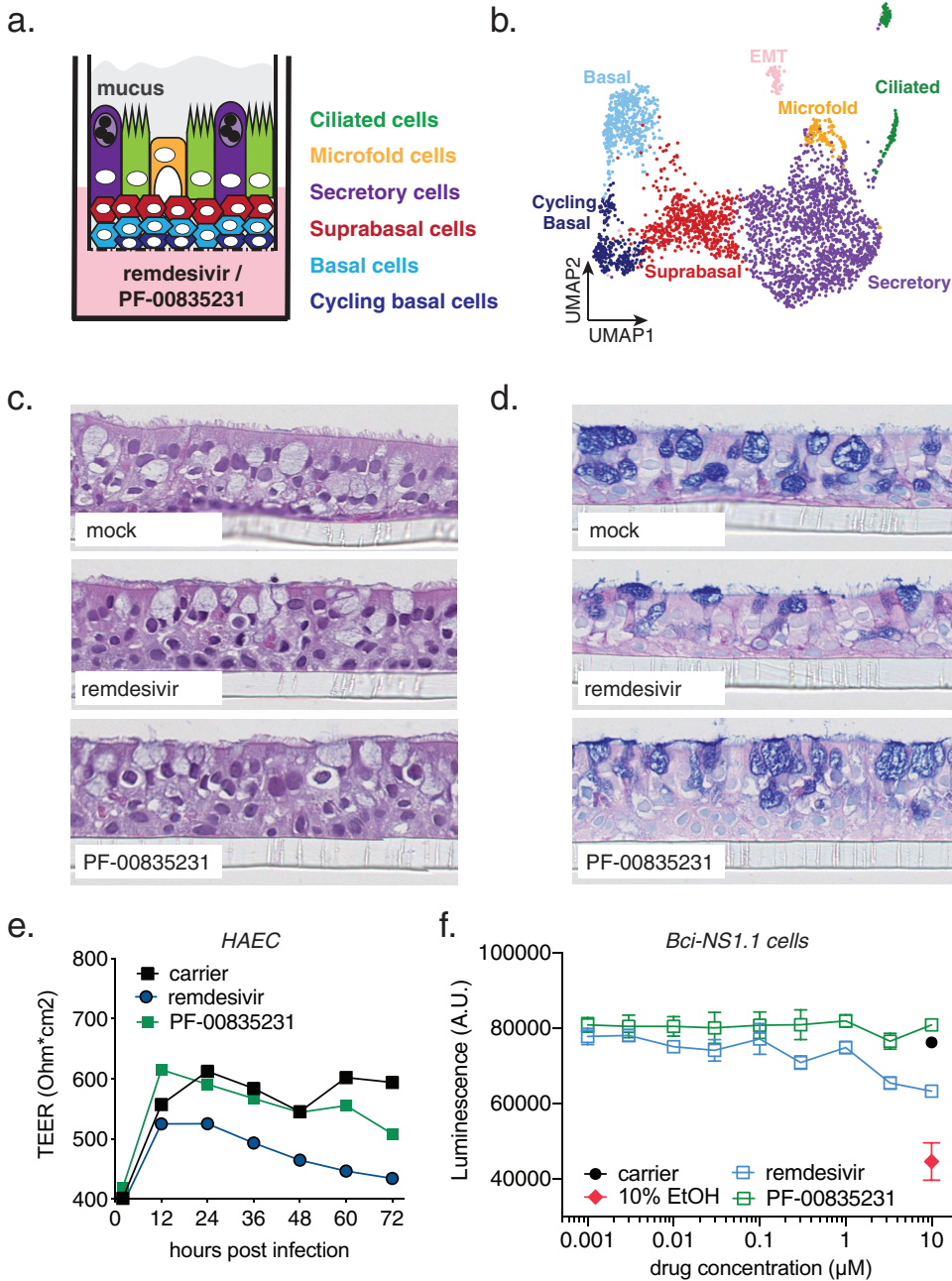
FIG 5 Cell composition of polarized human airway epithelial cultures (HAEC) and cytotoxicity of PF-00835231 and remdesivir. (a) Schematic representation of a transwell containing a polarized HAEC in air-liquid interface. Dark blue, cycling basal cells; light blue, basal cells; red, suprabasal cells; purple, secretory cells; yellow, microfold cells; green, ciliated cells; gray, mucus. To test for cytotoxicity, drugs were added to the medium in the basolateral chamber. (b) Clustered uniform manifold approximation and projection (UMAP) of single cells determined by single-cell RNA sequencing from $n = 3$ uninfected HAEC. Clusters were determined by markers from the literature (37, 38) and by differentially expressed marker genes for each cluster determined by Wilcoxon test. (c and d) Representative cross-sections of uninfected HAEC at 72 h post treatment with 10 μM PF-00835231 or 10 μM remdesivir. Hematoxylin and eosin (H&E) (c) or periodic acid-Schiff (PAS)–alcian blue toe staining (d). (e) Transepithelial resistance (TEER) in drug-treated, uninfected HAEC over time as a measure of epithelial integrity. Means $\pm$ SEM from $n = 3$ independent experiments. (f) CellTiter-Glo assay on undifferentiated, basal-like Bci-NS1.1 precursor cells. Means $\pm$ SEM from $n = 3$ independent experiments.
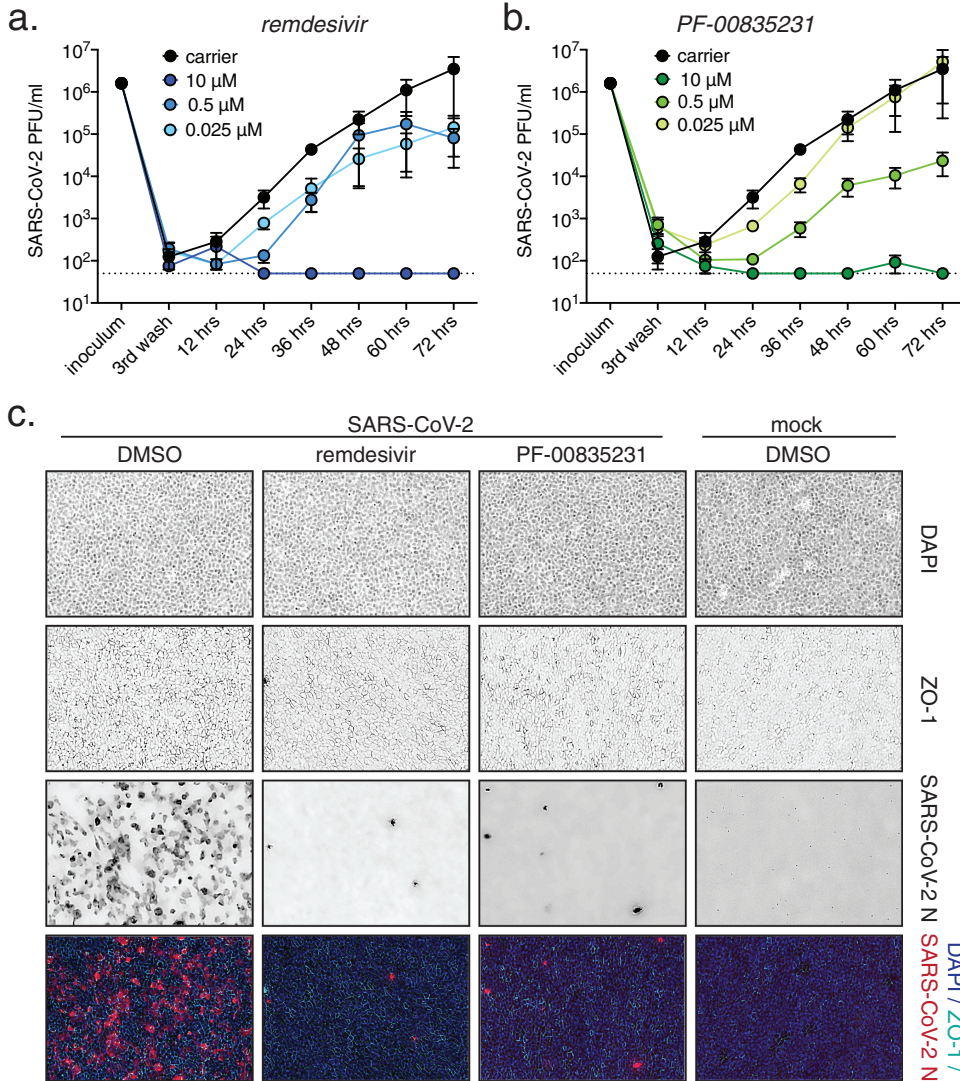
FIG 6 Comparative anti-SARS-CoV-2 activity of PF-00835231 and remdesivir in polarized human airway epithelial cultures (HAEC). To test for antiviral activity, drugs were added to the basolateral chamber, cultures were infected with SARS-CoV-2 from the apical side, and apical washes were collected in 12-h increments to determine viral titers by plaque assay. (a and b) SARS-CoV-2 USA-WA1/2020 infectious titers from HAEC treated with incremental doses of remdesivir (a) or PF-00835231 (b). (c) Representative top views of HAEC at 72 hpi; drug doses, 0.3 μM. Blue, 4′,6-diamidino-2-phenylindole (DAPI; nuclei); cyan, ZO-1 (tight junctions); red, SARS-CoV-2 N protein (infected).

10 μM PF-00835231 or remdesivir, we found in both cases that the number of infected cells was significantly reduced. Our results show that both remdesivir and PF-00835231 potently inhibit SARS-CoV-2 infection in our model of polarized human airway epithelium.

Inhibiting the multidrug transporter MDR1 does not increase the efficacy of PF-00835231 in human airway epithelial cells. Previously, a hurdle in accurately determining PF-00835231's *in vitro* efficacy was the action of the multidrug efflux transporter P-glycoprotein (also known as MDR1 or *ABCB1*). However, these earlier studies were performed in the monkey kidney cell line Vero E6 (9, 14). MDR1 was found to efficiently export PF-00835231, thereby reducing intracellular PF-00835231 levels and likely underestimating PF-00835231's potency. In those studies, chemical inhibition of MDR1 in Vero E6 cells significantly increased PF-00835231's antiviral efficacy (9, 14).

Given the previously reported species differences in P-glycoprotein-mediated drug transport activity of MDR1 and the variability in expression levels of the *ABCB1* gene that encodes this drug transporter among cell types and tissues (40), we sought to

determine a potential role of MDR1 in our human *in vitro* airway models. We measured PF-00835231 anti-SARS-CoV-2 activity while chemically blocking MDR1 function, using the drug CP-100356 in the A549^{+ACE2} cell line and in HAEC (Fig. 7a). We observed no changes in antiviral efficacy when blocking MDR1 activity (Fig. 7b to d), suggesting that, in contrast to Vero E6 cells, this transporter does not play a role in our human airway model systems. Indeed, scRNA-seq analysis of HAEC (Fig. 5b) (36) did not reveal any detectable MDR1 (*ABCB1*) transcripts, suggesting levels of this transporter in HAEC are low.

A limitation of the previous experiments is that A549 cells originate from one patient, and HAEC were differentiated from precursor cells obtained from a single donor (41). As a result, we cannot exclude the possibility that human genetic variation might influence MDR1 function or expression. Single-nucleotide polymorphisms (SNPs) in the *ABCB1* promoter or within the open reading frame are well described in the literature (15). Furthermore, an inherent limitation of sc-RNAseq is that only abundant transcripts are detected, and given the limited cellular heterogeneity of HAEC, it is possible that *ABCB1* transcripts remained undetected due to the limited depth of sequencing at the single cell level.

To address these issues, we investigated transcript levels of *ABCB1* in bronchoalveolar lavage (BAL) samples from healthy individuals and from COVID-19 patients with mild or severe symptoms from a previously published data set (42, 43). BAL samples contained multiple cell types, including airway epithelial cells, but also immune cells, such as macrophages, T cells, plasma cells, and neutrophils (Fig. 7e). In healthy individuals, we detected MDR1 (*ABCB1*) in 1.77% of CD8$^+$/NK cells, 0.59% of proliferating T cells, and 0.06% of alveolar macrophages, but not in other cell types. Notably, we did not observe any *ABCB1* transcripts in airway epithelial cells, which are thought to be the major site of SARS-CoV-2 replication (17, 18, 44, 45). Compared to BAL samples from healthy individuals, BAL samples from COVID-19 patients with mild or severe symptoms showed an increased number of cells with detectable levels of MDR1 (*ABCB1*) transcripts (Fig. 7f). Interestingly, rather than an overall increase in *ABCB1* gene expression, this upregulation was limited to a small subset of individual cells, with the majority of cells remaining *ABCB1* negative. This phenomenon was observed in alveolar macrophages (0.25%/0.28% positive in mild/severe COVID-19 patients), SPP1+ macrophages (0.23%/0.23%), M1-like macrophages (2.60%/0.43%), CD8$^+$/NK cells (7.75%/4.18%), proliferating T cells (2.00%/3.60%), plasma cells (cells not detected/0.74%), neutrophils (0%/0.05%), and epithelial cells (0.29%/0.18%). Our findings suggest that although MDR1 (*ABCB1*) is upregulated in some cells during inflammatory processes such as those observed in COVID-19, its expression remains cell type specific, and only a small fraction of airway epithelial cells, the main replication sites for SARS-CoV-2, exhibit detectable levels of this efflux transporter.

Thus, we conclude that MDR1 is unlikely to significantly impact PF-00835231 efficacy during SARS-CoV-2 infection of the respiratory epithelium. In addition, our findings highlight the importance of using appropriate *in vitro* models for the evaluation of antiviral drugs.

DISCUSSION

The current public health emergency caused by COVID-19 has illustrated our dire need for vaccines and therapeutics to combat SARS-CoV-2. The SARS-CoV-2 polymerase complex is the target of the majority of small-molecule inhibitors in multiple stages of development, including remdesivir (31), favipiravir (20), and β-D-N4-hydroxycytidine (46). At the time of writing, remdesivir is the only antiviral drug authorized for the treatment of COVID-19. In contrast to the above-mentioned compounds, PF-00835231 blocks the SARS-CoV-2 3CL^{pro} protease (9). PF-00835231 is the active component of PF-07304814, a first-in-class SARS-CoV-2 3CL^{pro} inhibitor currently in clinical trials. Here, we report the potent antiviral activity of PF-00835231 against SARS-CoV-2 in human lung epithelial cells and a model of polarized human airway epithelial cultures (HAEC). In our A549^{+ACE2} cell assay, we show that PF-00835231 has at least similar or better
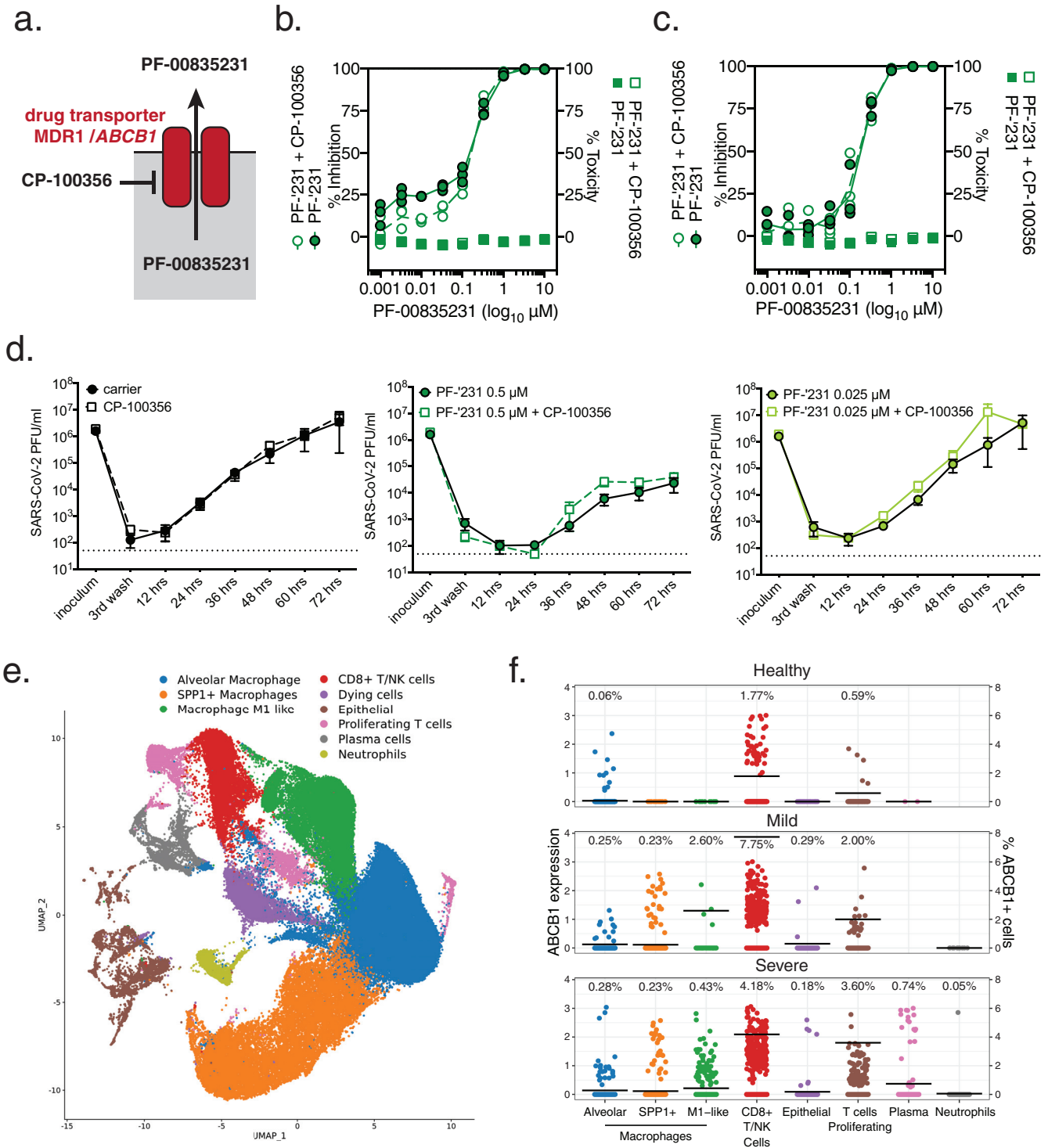
FIG 7 Role of MDR1 drug efflux transporter for PF-00835231-mediated SARS-CoV-2 inhibition in human airway cells. (a) Schematic of experimental setup for panels b to d. MDR1, encoded by open reading frame (ORF) *ABCB1*, exports PF-00835231 from cells. CP-100356 was used as a chemical inhibitor to block MDR1 function. (b and c) PF-00835231 antiviral activity and cytotoxicity in A549^{+ACE2} cells infected with SARS-CoV-2 USA-WA1/2020 for 24 (b), or 48 hpi (c) in the presence or absence of $1\,\mu$M MDR1 inhibitor CP-100356. Means $\pm$ SEM from $n=3$ independent experiments. (d) Apical SARS-CoV-2 USA-WA1/2020 infectious titers from HAEC treated basolaterally with 0, 0.025, or 0.5$\,\mu$M PF-00835231 in the presence or absence of $1\,\mu$M MDR1 inhibitor CP-100356. Means $\pm$ SEM from $n=3$ independent experiments. (e) Clustered UMAP of single cells from bronchoalveolar lavages of $n=12$ patients. Integrated data of healthy patients ($n=3$) and COVID-19 patients with mild ($n=3$) or severe ($n=6$) symptoms. (f) Normalized expression of *ABCB1* in clustered single cells from (e). Left y axis depicts the level of ABCB1 expression; right y axis depicts % of ABCB1-positive cells, also indicated by black bars; % of cells within each population with detectable ABCB1 transcripts is shown above for each population.

potency than the preclinical 3CL^{pro} inhibitor GC-376 or remdesivir. In HAEC, we found both remdesivir and PF-00835231 similarly potent.

The lack of inhibitors specific to SARS-CoV-2 early in the pandemic prompted off-label testing of protease inhibitors approved for other viruses, albeit with limited success (47). This failure highlighted the need for novel compounds of greater specificity. A number of 3CL^{pro} inhibitors have since been identified and characterized in *in vitro* assays, including the cancer drug carmofur (1-hexylcarbamoyl-5-fluorouracil) (12), an alpha-ketoamide inhibitor named 13b (7), and a dipeptide-based inhibitor named GC-376 (11). GC-376, licensed for veterinary use (29), was recently shown to inhibit SARS-CoV-2 in Vero E6 cells at an EC$_{50}$ of 0.9 μM (11). A different study showed that PF-00835231 inhibited SARS-CoV-2 at an EC$_{50}$ of 0.27 μM in Vero E6 cells (9). As such a comparison of historical data is problematic, we directly compared the antiviral efficacy of PF-00835231 and GC-376 side by side in the same assay (Fig. 3). We found that PF-00835231 is more potent that GC-376 in inhibiting SARS-CoV-2 and protecting cells from CPE. This result illustrates the *in vitro* potency of PF-00835231 compared to other, preclinical, 3CL^{pro} inhibitors, such as GC-376.

In coronaviruses, the genetic barrier to the standard-of-care remdesivir or the preclinical drug β-D-N4-hydroxycytidine is high, as mutations conferring resistance significantly reduce viral fitness, and cross-resistance between remdesivir or β-D-N4-hydroxycytidine has not been documented (33, 46). A high resistance barrier to 3CL^{pro}-targeting drugs due to a high fitness cost has also been demonstrated for the betacoronavirus murine hepatitis virus (MHV) (48). Although the likelihood of selecting for resistant variants thus seems low, the existence of drugs with alternate targets may have important advantages. First, as seen in other acute and chronic viral infections, blocking multiple targets in combination therapy further decreases the likelihood for selection of viral resistance mutants (49–51). Second, combination therapy with a cocktail of multiple drugs tackling different steps of the viral life cycle may have synergistic effects on controlling viral replication. Indeed, a recent *in vitro* study demonstrated significant synergistic effects between PF-00835231 and remdesivir in inhibiting SARS-CoV-2 (14). Third, upon failure of monotherapy, it is preferable to switch to an antiviral with a different target to circumvent cross-resistance caused by mutations in the same target (49–51). For these reasons, the development of a diverse toolbox of antiviral drugs with different targets will be important to improve antiviral therapy in COVID-19.

The optimal window of opportunity for starting a successful antiviral drug regimen during acute viral infections, such as influenza, is the first few days post symptom onset, while viral replication is actively ongoing (52). For most COVID-19 patients, this window is likely limited to the first week of symptoms (53). Such early treatment with remdesivir is impeded by its need for intravenous (i.v.) administration, requiring a health care facility setting, though it still demonstrated benefit for 68% of patients with more advanced infection in randomized clinical studies (54). PF-07304814, with its active component PF-00835231 evaluated in this study, is also an i.v. treatment (9). However, the time of active SARS-CoV-2 replication might be prolonged in the most severe patients, as suggested by the aforementioned clinical data for remdesivir (54). This suggests the usefulness of SARS-CoV-2 antiviral regimens even at later times of infection, which further supports the investigation of PF-00835231 for the treatment of COVID-19.

P-glycoprotein (also known as MDR1, and encoded by gene *ABCB1*) (9), is a membrane-associated ATP-dependent efflux pump capable of removing cytostatic drugs from target cells. The endogenous function of this transporter remains to be fully elucidated, but it is expressed across several immune cell types and other metabolically active cells. P-glycoprotein appears to be critical for maintenance and effector function of a range of cytotoxic immune cells (55–58). Two recent studies suggested that PF-00835231 is a substrate for P-glycoprotein. This might pose a concern regarding the bioavailability of PF-00835231 in SARS-CoV-2-infected cells. We addressed this concern in two ways, as follows: functionally, by using chemical inhibition of MDR1 in human

airway models, and transcriptionally, by determining the expression of *ABCB1* in HAEC or in cells obtained from BAL of healthy or COVID-19 patients. Our combined results demonstrate that MDR1 function does not impact PF-00835231 efficacy in our model systems, and it is expressed at very low levels in airway epithelial cells, which are the major sites of SARS-CoV-2 replication (17, 18, 44, 45). By mining scRNA-seq data from BAL samples of COVID-19 patients and healthy controls ($n = 12$) for *ABCB1* expression, we considered the genetic variability on the *ABCB1* locus beyond that present in our two model systems. Indeed, a number of SNPs have been shown to alter expression of *ABCB1* transcripts, either by changing transcription factor or micro-RNA binding sites upstream of the *ABCB1* open reading frame, or by enhancing mRNA transcription due to silent mutations within the *ABCB1* open reading frame (15). Other, missense, mutations within the *ABCB1* open reading frame have been shown to alter the functionality of MDR1, i.e., by altering membrane localization or recycling of the protein, or by modifying substrate recognition sites (15, 59). Although we do not have information on the *ABCB1* genotype of our mined patient samples, the detected low expression of *ABCB1* transcripts in the cells permissive for SARS-CoV-2, together with the functional data from our model system, instills confidence that PF-00835231 efficacy is not hampered by the action of MDR1.

Spillovers of zoonotic coronaviruses with high pathogenic potential into the human population are not isolated events, as repeatedly illustrated by the emergence of SARS-CoV in 2002, Middle East respiratory syndrome coronavirus (MERS-CoV) in 2012, and now SARS-CoV-2 in 2019 (60). To prepare for future pandemics, the development of pancoronavirus compounds is of strategic importance. This involves choosing viral targets that are highly conserved within the coronavirus family, such as the 3CL^pro protease (7). Indeed, a recent study performing *in vitro* protease activity assays with PF-00835231 revealed potent inhibition across a panel of diverse coronavirus 3CL^pro, including those of alphacoronaviruses (human coronavirus NL63, porcine epidemic diarrhea virus [PEDV], and feline infectious peritonitis virus [FIPV]), betacoronaviruses (Tylonycteris bat coronavirus HKU4, Pipistrellus bat coronavirus, HKU5, Rousettus bat coronavirus, HKU9, murine coronavirus [MHV], human coronavirus OC43, and human coronavirus HKU1), and a gammacoronavirus (avian infectious bronchitis virus [IBV]) (14). Our study revealed that the two 3CL^pro inhibitors tested (PF-00835231 and GC-376) were similarly potent for different clades of SARS-CoV-2 in which 3CL^pro is 100% conserved. It is of note that 3CL^pro is also 100% conserved in the SARS-CoV-2 "UK variant" B.1.1.7 and the "Brazil variant" B.1.1.28, whereas the "South African variant" B.1.352 carries amino acid substitution K90R (61–63). However, the K90 residue is distant from the active center of the protease and is not expected to influence 3CL^pro substrate specificity. These findings support the notion that PF-00835231 is an inhibitor with broad coronavirus activity, which may be of use for emerging SARS-CoV-2 variants and for other emerging coronaviruses beyond SARS-CoV-2.

Together, our data from two human *in vitro* model systems for SARS-CoV-2 show efficient PF-00835231 antiviral activity and mitigate concerns arising from nonhuman models such as Vero E6 cells regarding PF-00835231 counteraction by the efflux transporter P-glycoprotein. Our results therefore inform and reinforce the ongoing clinical studies of the prodrug PF-07304814 and its active form, PF-00835231, as a potential new treatment for COVID-19.

MATERIALS AND METHODS

Study design. The primary goal of this study was to compare the *in vitro* efficacy and cytotoxicity of PF-00835231 and remdesivir in two human model systems for SARS-CoV-2 infection, A549^+ACE2 cells and polarized human airway epithelial cultures. Compound characterization at NYU was done in a blind manner. If not stated otherwise, all assays were performed in biological replicates ($n = 3$). First, we performed in-depth characterization of A549^+ACE2 cells for the study of SARS-CoV-2, using RT-qPCR, Western blotting, flow cytometry, microscopy, and high-content imaging. Second, we evaluated the *in vitro* efficacy and cytotoxicity of PF-00835231; of a second, preclinical, protease inhibitor, GC-376; and of remdesivir in A549^+ACE2 cells. We performed antiviral assays with SARS-CoV-2 from the two major clades during the first year of the COVID-19 pandemic. Third, we performed time-of-drug-addition assays in

A549^{+ACE2} cells to delineate the time of antiviral action for PF-00835231, remdesivir, and GC-376 within the SARS-CoV-2 life cycle. Fourth, we assessed the *in vitro* efficacy and cytotoxicity of PF-00835231 and remdesivir in the physiologically relevant model of polarized human airway epithelial cultures. Finally, we determined the role of efflux transporter MDR1 on the antiviral efficacy of PF-00835231. Our studies were intended to generate the data required to assess further preclinical investigations and the launch of a phase 1b clinical trial with PF-00835231 as a base compound for the potential treatment of COVID-19.

Cells and viruses. A549 cells were purchased from ATCC (catalog [cat.] no. CCL-185). To generate A549^{+ACE2} cells, we cloned the human ACE2 cDNA sequence (GenBank accession number NP_001358344.1) into a pLV-EF1a-IRES-Puro backbone vector (cat. no. 85132; Addgene), and prepared lentiviral particles as described previously (64). A549 cells were transduced with pLV-EF1α-hACE2-IRES-Puro lentivirus and bulk selected for transduced cells using 2.5 μg/ml puromycin. A549^{+ACE2} cells were maintained in Dulbecco's modified Eagle's medium (DMEM; cat. no. 11965-092; Gibco) containing 10% fetal bovine serum (FBS, cat. no. S11150; Atlanta Biologicals) (complete medium), and puromycin (2.5 μg/ml final) was added to the medium at every other passage. A549^{+ACE2} cells were used for SARS-CoV-2 infection studies. Vero E6 cells, purchased from ATCC (cat. no. CLR-1586), were maintained in DMEM (cat. no. 11965-092; Gibco) containing 10% FBS (cat. no. S11150; Atlanta Biologicals), and were used for growing SARS-CoV-2 stocks and for SARS-CoV-2 plaque assays. Basal-like human airway progenitor cells (Bci-NS1.1 [41]) were obtained from Ronald G. Crystal and were used for cytotoxicity assays and for the generation of polarized human airway epithelial cultures (HAEC). They were maintained in BEGM medium (cat. no. CC-3171 and CC-4175; Lonza) for cytotoxicity assays, while Pneumacult-Ex Plus medium (cat. no. 05040; Stemcell Technologies) was used to culture Bci-NS1.1 cells for the generation of human airway epithelial cultures.

All SARS-CoV-2 stock preparations and subsequent infection assays were performed in the CDC/USDA-approved biosafety level 3 (BSL-3) facility in compliance with NYU Grossman School of Medicine guidelines for BSL-3. SARS-CoV-2 isolate USA-WA1/2020, deposited by the Centers for Disease Control and Prevention, was obtained through BEI Resources, NIAID, NIH (cat. no. NR-52281; GenBank accession number MT233526). The USA-WA1/2020 stock, obtained at passage 4, was passaged once in Vero E6 cells to generate a passage 5 working stock (1.7E+06 PFU/ml) for our studies on A549^{+ACE2}. For studies on human airway epithelial cultures, passage 5 USA-WA1/2020 was amplified once more in Vero E6 cells and concentrated using an Amicon Ultra-15 centrifugal filter unit with a cut off 100 kDa, resulting in a passage 6 working stock of 1.08E+07 PFU/ml. SARS-CoV-2 USA/NYU-VC-003/2020 was isolated from patient nasal swab material in March 2020 (GenBank accession number MT703677). We inoculated Vero E6 cells with a 1:2 dilution series of the nasal swab material in infection media (DMEM, 2% FBS, 1% penicillin-streptomycin [Pen-Strep], 1% nonessential amino acids [NEAA], and 10 mM HEPES) to obtain passage 0 (P0) stock. P0 was passaged twice in Vero E6 to generate a passage 2 working stock (1.1E+07 PFU/ml) for drug efficacy studies on A549^{+ACE2}. For viral growth kinetics, pooled medium from P0 stock was used to plaque purify a single virus clone on Vero E6 cells in the presence of 1 μg/ml L-1-tosyla-mido-2-phenylethyl chloromethyl ketone (TPCK)-trypsin, to avoid virus adaptation to Vero E6 cells due to the lack of TMPRSS2 expression (65). Purified plaques were sequenced to verify the signature clade B amino acid changes, S D614G and NSP12 P323L, before expanding in the presence of TPCK-trypsin to generate a passage 1 working stock (1.8 E+06 PFU/ml).

Characterization of A549^{+ACE2} cells. Confluent 6-well A549 and A549^{+ACE2} cells were washed with phosphate-buffered saline (PBS), and cells were detached with CellStripper dissociation reagent (cat. no. 25056Cl; Corning). Cells were pelleted, washed with PBS, and either (i) lysed in LDS sample buffer (cat no. NP0007; Thermo Fisher) supplemented with reducing agent (cat. no. NP0004; Thermo Fisher), after which Western blots were performed to analyze ACE2 (1:1,000, cat. no. GTX101395; GeneTex) with beta-actin (1:10,000, cat. no. MA5-15739; Thermo Fisher) as the loading control and imaged using a Li-Cor Odyssey CLx system, or (ii) incubated in fluorescence-activated cell sorting (FACS) buffer (PBS, 5% FBS, 0.1% sodium azide, and 1 mM EDTA) for 30 min on ice followed by 1 h incubation with Alexa Fluor 647 conjugated anti-ACE2 (1:40, cat. no. FABAF9332R; R&D Biosystems) or isotype control (1:40, cat. no. IC003R; R&D Biosystems) and subsequent analysis on a CytoFlex flow cytometer. Surface ACE2 was visualized by staining A549 and A549^{+ACE2} cells at 4°C with anti-ACE2 (1:500, cat. no. AF933; R&D Biosystems) and Alexa Fluor 647 secondary antibody and 4',6-diamidino-2-phenylindole (DAPI). Images were collected on the BZ-X810 fluorescence microscope (RRID:SCR_016979; Keyence, Osaka, Japan).

Confluent 6-well A549 and A549^{+ACE2} cells were collected in RLT lysis buffer supplemented with beta-mercaptoethanol, and total RNA was extracted using a Qiagen RNeasy minikit. cDNA synthesis was performed using the SuperScript III system (cat. no. 18080051; Thermo Fisher) followed by RT-qPCR with PowerUp SYBR green mastermix (cat. no. A25742; Thermo Fisher) on a QuantStudio 3 real-time PCR system using gene-specific primers pairs for ACE2 and RPS11 as the reference gene. (ACE2fwd, GGGATCAGAGATCGGAAGAAGAAA; ACE2rev, AGGAGGTCTGAACATCATCAGTG; RPS11fwd, GCCGAGACTATCTGCACTAC; and RPS11rev, ATGTCCAGCCTCAGAACTTC). A549 and A549^{+ACE2} cells were seeded in black-walled 96-well plates, and at confluence, cells were infected with SARS-CoV-2. At 24 and 48 hpi, samples were fixed, stained with mouse monoclonal SARS-CoV anti-N antibody 1C7, which cross-reacts with SARS-CoV-2 N (1:1,000, kind gift of Thomas Moran), Alexa Fluor 647 secondary antibody, and DAPI, and imaged using the CellInsight CX7 LZR high-content screening platform. Images were analyzed and quantified with HCS Navigator software. Syncytia were imaged using the Keyence BZ-X810 microscope at ×60 magnification on A549^{+ACE2} cultured on chambered slides followed by 48 hpi SARS-CoV-2 infection and staining with SARS-CoV-2 N, Alexa Fluor 647 secondary antibody, and DAPI.

SARS-CoV-2 growth kinetics on A549^{+ACE2} cells. A549^{+ACE2} cells were seeded into 6-cm dishes at 70% confluence. The next day, medium was removed, and cells were washed twice with PBS with calcium and magnesium to remove residual medium. Cells were then infected at a 0.01 multiplicity of

infection (MOI), based on A549^{+ACE2} titer, at 37°C. The remaining inoculum was stored at -80°C for back titration. At 1 h post virus addition, virus was removed, cells were washed twice with PBS with calcium and magnesium to remove unbound virus, and infection media (DMEM, 2% FBS, 1% Pen-Strep, 1% NEAA, 10 mM HEPES) was added. 60 μl of supernatant were collected and stored at -80°C to determine successful removal of input virus. Supernatant was then collected at 12, 24, 48, and 72 hpi, and stored at -80°C.

Viral titers in the supernatants were determined by focus-forming assay. A549^{+ACE2} cells were seeded into black-walled 96-well plates at 70% confluence. The next day, cells were then infected with 1:10 serial dilutions of the collected samples for 1 h at 37°C. At 1 h post virus addition, virus was removed, and cells were overlaid with minimal essential medium (MEM) 1.8% Avicell, 1% Pen-Strep, 1% GlutaMax, 20 mM HEPES, 0.4% BSA, and 0.24% NaHCO$_3$. At 48 h postinfection, the overlay was removed, and cells were fixed by submerging in 10% formalin solution for 30 to 45 min. After fixation, cells were washed once with H$_2$O to remove excess formalin. Plates were dried, and PBS was added to each well before plates exited the BSL-3 facility. Fixed cells were permeabilized with Triton-X and stained with mouse monoclonal SARS-CoV anti-N antibody 1C7, which cross-reacts with SARS-CoV-2 N (kind gift of Thomas Moran), goat anti-mouse Alexa Fluor 647, and DAPI. Plates were scanned on the CellInsight CX7 LZR high-content screening platform. A total of 9 images were collected at ×4 magnification to span the entire well. Infection foci were counted manually.

Human airway epithelial cultures. To generate HAEC, Bci-NS1.1 were plated (7.5 E+04 cells/well) on rat tail collagen type 1-coated permeable transwell membrane supports (6.5 mm, cat. no. 3470; Corning), and immersed apically and basolaterally in Pneumacult-Ex Plus medium (cat. no. 05040; Stemcell Technologies). Upon reaching confluence, medium was removed from the apical side ("airlift"), and medium in the basolateral chamber was changed to Pneumacult ALI maintenance medium (cat. no. 05001; Stemcell Technologies). Medium in the basolateral chamber was exchanged with fresh Pneumacult ALI maintenance medium every 2 to 3 days for 12 to 15 days to form differentiated, polarized cultures that resemble *in vivo* pseudostratified mucociliary epithelium. Cultures were used within 4 to 6 weeks of differentiation. HAEC were used for cytotoxicity assays and SARS-CoV-2 infections.

Compound acquisition, dilution, and preparation. PF-00835231, remdesivir, and CP-100356 were solubilized in 100% DMSO and were provided by Pfizer, Inc. Compound stocks diluted in DMSO to 30 mM were stored at -20°C. Compounds were diluted to 10 μM working concentration in complete medium or in Pneumacult ALI maintenance medium. All subsequent compound dilutions were performed in according medium containing DMSO equivalent to 10 μM compound. GC-376 was purchased from BPS Biosciences (cat. no. 78013) and used at 10 μM working concentration. SARS-CoV-2 (2019-nCov) rabbit polyclonal spike-neutralizing antibody from Sino Biological (cat. no. 40592-R001) was used at 3 μM working concentration. As a positive control for cytotoxicity assays, staurosporine was purchased from Sigma (cat. no. S6942) and used at 1 μM working concentration.

In vitro drug efficacy and cytotoxicity in A549^{+ACE2} cells. A549^{+ACE2} cells were seeded into black-walled 96-well plates at 70% confluence. The next day, medium was removed and replaced with complete medium containing compound/carrier 2 h prior to infection. Cells were then infected at a 0.425 multiplicity of infection (MOI), based on Vero E6 titer, at 37°C. At 1 h post virus addition, virus was removed, and medium containing compound/carrier was added. At 24 and 48 h postinfection, cells were fixed by submerging in 10% formalin solution for 30 to 45 min. After fixation, cells were washed once with H$_2$O to remove excess formalin. Plates were dried, and PBS was added to each well before plated exited the BSL-3 facility. Fixed cells were permeabilized with Triton-X and stained with mouse monoclonal SARS-CoV anti-N antibody 1C7, which cross-reacts with SARS-CoV-2 N (kind gift of Thomas Moran), goat anti-mouse Alexa Fluor 647, and DAPI. Plates were scanned on the CellInsight CX7 LZR high-content screening platform. A total of 9 images were collected at ×4 magnification to span the entire well. Images were analyzed using HCS Navigator to obtain the total number of cells/well (DAPI-stained cells) and the percentage of SARS-CoV-2 infected cells (Alexa Fluor 647 positive cells). To enable accurate quantification, exposure times for each channel were adjusted to 25% of saturation, and cells at the edge of each image were excluded from the analysis. SARS-CoV-2-infected cells were gated to include cells with an average fluorescence intensity greater than 3 standard deviations that of mock-infected and carrier-treated cells. Representative images of viral foci were acquired using the BZ-X810 at ×40 magnification of plates fixed at 48 hpi SARS-CoV-2 infection.

For determination of cytotoxicity, A549^{+ACE2} cells were seeded into opaque white-walled 96-well plates. The following day, medium was removed, replaced with medium containing compound/carrier or staurosporine, and incubated for 24 or 48 h, respectively. At these time points, ATP levels were determined by CellTiter-Glo 2.0 (cat. no. G9242; Promega) using a BioTek Synergy HTX multimode reader.

Time-of-drug-addition experiments. A549^{+ACE2} cells seeded into black-walled 96-well plates and at confluence were treated and infected as followed. At 2.5 h prior infection, cells were pretreated with complete medium containing 1× compound/carrier. In addition, SARS-CoV-2 (2×) was incubated with SARS-CoV-2 (2019-nCov) rabbit polyclonal spike-neutralizing antibody (NAb; 2×). Pretreated cells and virus/neutralizing antibody mix (1×) were incubated for 1 h at 37°C. To synchronize infection, preincubated plates and SARS-CoV-2/NAb mix were chilled at 4°C for 30 min, and SARS-CoV-2 was diluted on ice in medium containing compound/carrier/NAb. Following prechilling, virus/compound/carrier/NAb mixtures were added to the cells to allow binding of virus for 1 h at 4°C. Plates were moved to 37°C to induce virus entry and therefore infection. At 1 h post virus addition, virus was removed, and complete medium was added to all wells. Complete medium containing 2× compound/carrier/NAb was added to pretreated cells, cells treated at infection, and cells treated at 1 h postinfection. At 2, 3, and 4 h postinfection, complete medium containing compound/carrier/NAb was added to the according wells. At 12 h

postinfection, samples were fixed, stained with SARS-CoV-2 N, Alexa Fluor 647 secondary antibody, and DAPI, and imaged using the CellInsight CX7 LZR high-content screening platform. Images were analyzed and quantified with HCS Navigator software as described for *in vitro* efficacy in A549^{+ACE2}.

In vitro efficacy and cytotoxicity in human airway epithelial cultures. At 48 h prior to infection, 2- to 6-week-old HAEC were washed apically twice for 30 min each with prewarmed PBS containing calcium and magnesium, to remove mucus on the apical surface. At 2 h prior to infection, HAEC were pretreated by exchanging the ALI maintenance medium in the basal chamber with fresh medium containing compounds or carrier. Remdesivir and PF-00835231 were used at 10, 0.5, and 0.025 μM, and CP-100356 at 1 μM. At 1 h prior to infection, cultures were washed apically twice for 30 min each with prewarmed PBS containing calcium and magnesium. Each culture was infected with 1.35E+05 PFU (Vero E6) per culture for 2 h at 37°C. A sample of the inoculum was kept and stored at −80°C for back titration by plaque assay on Vero E6 cells. For assessment of compound toxicity, additional cultures were washed and pretreated like the infected cultures. Instead of being infected, these cultures were incubated with PBS containing calcium and magnesium only as mock treatment. HAEC were incubated with the viral dilution or mock treatment for 2 h at 37°C. The inoculum was removed, and the cultures were washed three times with prewarmed PBS containing calcium and magnesium. For each washing step, buffer was added to the apical surface, and cultures were incubated at 37°C for 30 min before the buffer was removed. The third wash was collected and stored at −80°C for titration by plaque assay on Vero E6 cells. Infected cultures were incubated for a total of 72 h at 37°C. Infectious progeny virus was collected every 12 h by adding 60 μl of prewarmed PBS containing calcium and magnesium, incubation at 37°C for 30 min, and collection of the apical wash to store at −80°C until titration. Additionally, transepithelial electrical resistance (TEER) was measured in uninfected but treated HAEC to quantify the tissue integrity in response to treatment with compounds or carrier. At the endpoint, cultures were fixed by submerging in 10% formalin solution for 24 h and washed three times with PBS containing calcium and magnesium before further processing for histology. Alternatively, at the endpoint, transwell membranes were excised and submerged in RLT buffer to extract RNA using the RNeasy kit (cat. no. 74104; Qiagen). cDNA synthesis was performed using the SuperScript III system (cat. no. 18080051; Thermo Fisher), followed by RT-qPCR with TaqMan universal PCR master mix (cat. no. 4305719; Thermo Fisher) and TaqMan gene expression assay probes (GAPDH [cat no. 4333764F], BAX [cat no. Hs00180269_m1], and BCL2 [cat no. Hs00608023_m1]; Thermo Fisher) using a QuantStudio 3 real-time PCR system.

For additional determination of cytotoxicity in undifferentiated HAEC precursor cells, Bci-NS1.1 cells were seeded into opaque white-walled 96-well plates. The following day, medium was removed, replaced with medium containing compound/carrier or staurosporine, and incubated for 24 or 48 h, respectively. At these time points, ATP levels were determined by CellTiter-Glo 2.0 (cat. no. G9242; Promega) using a BioTek Synergy HTX multimode reader.

Histology on human airway epithelial cultures. For histology, transwell inserts were prepared using a Leica Peloris II automated tissue processor, paraffin embedded, and sectioned at 3 μm. The resulting slides were stained using a modified periodic acid-Schiff (PAS)–alcian blue protocol. Sections were imaged on the Leica SCN whole-slide scanner, and files were uploaded to the SlidePath Digital Image Hub database for viewing.

Immunofluorescence on human airway epithelial cultures. For immunofluorescence of HAEC at top view, fixed and washed cultures were permeabilized with 50 mM NH$_4$Cl (in PBS), 0.1% wt/vol saponin, and 2% BSA (permeabilization/blocking [PB] buffer). Cultures were stained with (i) rabbit polyclonal anti-SARS nucleocapsid protein antibody, which cross-reacts with SARS-CoV-2 N (1:1,000, cat. no. 200-401-A50; Rockland) and goat-anti-rabbit Alexa Fluor 488, to visualize infection, (ii) mouse monoclonal anti-ZO-1-1A12 (1:500, cat. no. 33-9100; Thermo Fisher) and goat anti-mouse Alexa Fluor 647 to visualize tight junctions, and (iii) DAPI. All dilutions were prepared in PB buffer. Images were collected on the Keyence BZ-X810 microscope.

Single-cell RNA-seq analysis of human airway epithelial cultures. Six-week-old human airway cultures were used for the single-cell RNA-seq analysis. The apical surface was washed once to remove mucus by adding 100 μl of PBS and incubating for 30 min at 37°C. Cells were dissociated by cutting out the transwell membrane and incubating it in 700 μl TrpLE 10× (cat. no. A1217701; Thermo Fisher) for 30 min with rocking at 37°C. To increase dissociation, cells were pipetted through wide-bore tips every 10 min during the incubation time. When cells were visually dissociated, 700 μl of ALI maintenance medium supplemented with 0.1% Pluronic (cat. no. 24040032; Thermo Fisher) was added, and cells were carefully pipetted again using wide-bore tips. The cell suspension was centrifuged through a 10-μm filter at 300 × g for 5 min to break up any remaining cell clumps. The cell pellet was washed once with 200 μl ALI maintenance medium supplemented with 0.1% Pluronic before cell number and viability were assed using the Countess II instrument (Thermo Fisher) to calculate cell numbers used in the following steps for single-cell RNA-seq analysis.

Single-cell transcriptome profiling of dissociated organoids was carried out using the Chromium Next GEM single-cell 5′ library and gel bead kit and Chromium Controller (10x Genomics). To enable multiplexing and doublet detection, cells were stained with barcoded antibodies described previously (66). Briefly, approximately 200,000 cells per sample were resuspended in staining buffer (PBS, 2% BSA, and 0.01% Tween) and incubated for 10 min with Fc block (TruStain FcX [BioLegend] and FcR blocking reagent [Miltenyi]). Cells were then incubated with barcoded hashing antibodies for 30 min at 4°C. After staining, cells were washed 3 times in staining buffer. After the final wash, cells were resuspended in PBS plus 0.04% BSA, filtered, and counted. Cells were pooled and loaded onto the chromium chips. For each lane, we pooled 5 samples (~10,000 cells per sample). The single-cell capturing, barcoding, and

cDNA library preparation were performed using the Chromium Next GEM single-cell 5' library and gel bead kit by following the protocols recommended by the manufacturer. Hashtag-oligonucleotide (HTO) additive oligonucleotide was spiked into the cDNA amplification PCR, and the HTO library was prepared as described previously (67).

The Cell Ranger software suite (10x Genomics) from was used to demultiplex cellular barcodes, align reads to the human genome (GRCh38 ensemble, http://useast.ensembl.org/Homo_sapiens/Info/Index) and perform unique molecular identifier (UMI) counting. From filtered counts, HTODemux was used to demultiplex hashtagged samples, and Seurat1 version 3.1.3 was used to process the single-cell data, including dimension reduction, uniform manifold approximation and projection (UMAP) representation, and differential expression, to identify cell type-specific markers determined by Wilcoxon test (68).

In silico analysis of bronchoalveolar lavage samples). Filtered gene-barcode matrices for the bronchoalveolar lavage (BAL) sample data set were downloaded from GEO accession number GSE145926. Matrices were normalized using "LogNormalize" methods in Seurat v.3 with default parameters, and the resulting values were scaled using ScaleData. Seurat v.3.1.3 was used to process the single-cell data, including dimension reduction, UMAP representation, and differential expression, to identify cell type-specific markers determined by Wilcoxon test.

Statistical analysis. Antiviral activities of PF-00835231 and remdesivir in A549^{+ACE2} cells were determined by the following method. The percent inhibition at each concentration was calculated by ActivityBase (IDBS) based on the values for the no-virus control wells and virus-containing control wells on each assay plate. The concentration required for a 50%/90% response (EC$_{50}$/EC$_{90}$) was determined from these data using a 4-parameter logistic model. Curves were fitted to a Hill slope of 3 when >3 and the top dose achieved ≥50% effect. Geometric means and 95% confidence intervals were generated in ActivityBase. Statistical comparisons were performed by log transforming the EC$_{50}$ and EC$_{90}$ values and fitting separate linear models to each endpoint, assuming equal log scale variances across conditions and interactions of compound with strain and compound with time. The model can be described mathematically as

$$\log EC_x = \text{treatment}_i + \varepsilon_{i,j}, x = 50 \text{ or } 90$$

where "treatment$_i$" represents the effect of the combination of compound, strain, and time and $\varepsilon_{i,j}$ represents a normal error term for treatment i and assay replicate j. Contrasts between the factor combinations of interest were computed to assess significance and back transformed into ratios of geometric means. Statistical significance was defined by a P value of <0.05. Other statistical data analyses were performed in GraphPad Prism 7. Statistical significance for each endpoint was determined with specific statistical tests, as indicated in each legend. For each test, a P value of <0.05 was considered statistically significant.

Data availability. All scRNA-seq data in this study can be accessed in the GEO database under accession numbers GSE166601 and GSE145926. All correspondence and material requests except those for antiviral compounds should be addressed to Meike Dittmann (Meike.Dittmann@nyulangone.org). Compound requests should be addressed to Annaliesa Anderson (Annaliesa.Anderson@pfizer.com).

REFERENCES

1. Zhu N, Zhang D, Wang W, Li X, Yang B, Song J, Zhao X, Huang B, Shi W, Lu R, Niu P, Zhan F, Ma X, Wang D, Xu W, Wu G, Gao GF, Tan W, China Novel Coronavirus Investigating and Research Team. 2020. A novel coronavirus from patients with pneumonia in China, 2019. N Engl J Med 382:727–733. https://doi.org/10.1056/NEJMoa2001017.

2. Gorbalenya AE, Baker SC, Baric RS, de Groot RJ, Drosten C, Gulyaeva AA, Haagmans BL, Lauber C, Leontovich AM, Neuman BW, Penzar D, Perlman S, Poon LLM, Samborskiy DV, Sidorov IA, Sola I, Ziebuhr J. 2020. The species *Severe acute respiratory syndrome-related coronavirus*: classifying 2019-nCoV and naming it SARS-CoV-2. Nat Microbiol 5:536–544. https://doi.org/10.1038/s41564-020-0695-z.

3. Pruijssers AJ, George AS, Schäfer A, Leist SR, Gralinksi LE, Dinnon KH, Yount BL, Agostini ML, Stevens LJ, Chappell JD, Lu X, Hughes TM, Gully K, Martinez DR, Brown AJ, Graham RL, Perry JK, Du Pont V, Pitts J, Ma B, Babusis D, Murakami E, Feng JY, Bilello JP, Porter DP, Cihlar T, Baric RS, Denison MR, Sheahan TP. 2020. Remdesivir inhibits SARS-CoV-2 in human lung cells and chimeric SARS-CoV expressing the SARS-CoV-2 RNA polymerase in mice. Cell Rep 32:107940. https://doi.org/10.1016/j.celrep.2020.107940.

4. Ziebuhr J, Siddell SG. 1999. Processing of the human coronavirus 229E replicase polyproteins by the virus-encoded 3C-like proteinase: identification of proteolytic products and cleavage sites common to pp1a and pp1ab. J Virol 73:177–185. https://doi.org/10.1128/JVI.73.1.177-185.1999.

5. Gadlage MJ, Denison MR. 2010. Exchange of the coronavirus replicase polyprotein cleavage sites alters protease specificity and processing. J Virol 84:6894–6898. https://doi.org/10.1128/JVI.00752-10.

6. Dai W, Zhang B, Jiang X-M, Su H, Li J, Zhao Y, Xie X, Jin Z, Peng J, Liu F, Li C, Li Y, Bai F, Wang H, Cheng X, Cen X, Hu S, Yang X, Wang J, Liu X, Xiao G, Jiang H, Rao Z, Zhang L-K, Xu Y, Yang H, Liu H. 2020. Structure-based design of antiviral drug candidates targeting the SARS-CoV-2 main protease. Science 368:1331–1335. https://doi.org/10.1126/science.abb4489.

7. Zhang L, Lin D, Sun X, Curth U, Drosten C, Sauerhering L, Becker S, Rox K, Hilgenfeld R. 2020. Crystal structure of SARS-CoV-2 main protease provides a basis for design of improved α-ketoamide inhibitors. Science 368:409–412. https://doi.org/10.1126/science.abb3405.

8. Gordon DE, Jang GM, Bouhaddou M, Xu J, Obernier K, White KM, O'Meara MJ, Rezelj VV, Guo JZ, Swaney DL, Tummino TA, Hüttenhain R, Kaake RM, Richards AL, Tutuncuoglu B, Foussard H, Batra J, Haas K, Modak M, Kim M, Haas P, Polacco BJ, Braberg H, Fabius JM, Eckhardt M, Soucheray M, Bennett MJ, Cakir M, McGregor MJ, Li Q, Meyer B, Roesch F, Vallet T, Mac Kain A, Miorin L, Moreno E, Naing ZZC, Zhou Y, Peng S, Shi Y, Zhang Z, Shen W, Kirby IT, Melnyk JE, Chorba JS, Lou K, Dai SA, Barrio-Hernandez I, Memon D, Hernandez-Armenta C, et al. 2020. A SARS-CoV-2 protein interaction map reveals targets for drug repurposing. Nature 583:459–468. https://doi.org/10.1038/s41586-020-2286-9.

9. Hoffman RL, Kania RS, Brothers MA, Davies JF, Ferre RA, Gajiwala KS, He M, Hogan RJ, Kozminski K, Li LY, Lockner JW, Lou J, Marra MT, Mitchell LJ, Murray BW, Nieman JA, Noell S, Planken SP, Rowe T, Ryan K, Smith GJ, Solowiej JE, Steppan CM, Taggart B. 2020. Discovery of ketone-based covalent inhibitors of coronavirus 3CL proteases for the potential therapeutic treatment of COVID-19. J Med Chem 63:12725–12747. https://doi.org/10.1021/acs.jmedchem.0c01063.

10. Yoshino R, Yasuo N, Sekijima M. 2020. Identification of key interactions between SARS-CoV-2 main protease and inhibitor drug candidates. Sci Rep 10:12493. https://doi.org/10.1038/s41598-020-69337-9.

11. Ma C, Sacco MD, Hurst B, Townsend JA, Hu Y, Szeto T, Zhang X, Tarbet B, Marty MT, Chen Y, Wang J. 2020. Boceprevir, GC-376, and calpain inhibitors II, XII inhibit SARS-CoV-2 viral replication by targeting the viral main protease. Cell Res 30:678–692. https://doi.org/10.1038/s41422-020-0356-z.

12. Jin Z, Zhao Y, Sun Y, Zhang B, Wang H, Wu Y, Zhu Y, Zhu C, Hu T, Du X, Duan Y, Yu J, Yang X, Yang X, Yang K, Liu X, Guddat LW, Xiao G, Zhang L, Yang H, Rao Z. 2020. Structural basis for the inhibition of SARS-CoV-2 main protease by antineoplastic drug carmofur. Nat Struct Mol Biol 27:529–532. https://doi.org/10.1038/s41594-020-0440-6.

13. Jin Z, Du X, Xu Y, Deng Y, Liu M, Zhao Y, Zhang B, Li X, Zhang L, Peng C, Duan Y, Yu J, Wang L, Yang K, Liu F, Jiang R, Yang X, You T, Liu X, Yang X, Bai F, Liu H, Liu X, Guddat LW, Xu W, Xiao G, Qin C, Shi Z, Jiang H, Rao Z, Yang H. 2020. Structure of Mpro from SARS-CoV-2 and discovery of its inhibitors. Nature 582:289–293. https://doi.org/10.1038/s41586-020-2223-y.

14. Boras B, Jones RM, Anson BJ, Arenson D, Aschenbrenner L, Bakowski MA, Beutler N, Binder J, Chen E, Eng H, Hammond J, Hoffman R, Kadar EP, Kania R, Kimoto E, Kirkpatrick MG, Lanyon L, Lendy EK, Lillis JR, Luthra SA, Ma C, Noell S, Obach RS, O'Brien MN, O'Connor R, Ogilvie K, Owen D, Pettersson M, Reese MR, Rogers T, Rossulek MI, Sathish JG, Steppan C, Ticehurst M, Updyke LW, Zhu Y, Wang J, Chatterjee AK, Mesecar AD, Anderson AS, Allerton C. 2020. Discovery of a novel inhibitor of coronavirus 3CL protease as a clinical candidate for the potential treatment of COVID-19. bioRxiv https://doi.org/10.1101/2020.09.12.293498.

15. Bossennec M, Di Roio A, Caux C, Ménétrier-Caux C. 2018. MDR1 in immunity: friend or foe? Oncoimmunology 7:e1499388-11. https://doi.org/10.1080/2162402X.2018.1499388.

16. Sankatsing SUC, Beijnen JH, Schinkel AH, Lange JMA, Prins JM. 2004. P glycoprotein in human immunodeficiency virus type 1 infection and therapy. Antimicrob Agents Chemother 48:1073–1081. https://doi.org/10.1128/AAC.48.4.1073-1081.2004.

17. Puelles VG, Lütgehetmann M, Lindenmeyer MT, Sperhake JP, Wong MN, Allweiss L, Chilla S, Heinemann A, Wanner N, Liu S, Braun F, Lu S, Pfefferle S, Schröder AS, Edler C, Gross O, Glatzel M, Wichmann D, Wiech T, Kluge S, Pueschel K, Aepfelbacher M, Huber TB. 2020. Multiorgan and renal tropism of SARS-CoV-2. N Engl J Med 383:590–592. https://doi.org/10.1056/NEJMc2011400.

18. Zou L, Ruan F, Huang M, Liang L, Huang H, Hong Z, Yu J, Kang M, Song Y, Xia J, Guo Q, Song T, He J, Yen H-L, Peiris M, Wu J. 2020. SARS-CoV-2 viral load in upper respiratory specimens of infected patients. N Engl J Med 382:1177–1179. https://doi.org/10.1056/NEJMc2001737.

19. Blanco-Melo D, Nilsson-Payant BE, Liu W-C, Uhl Hoagland SD, Møller R, Jordan TX, Oishi K, Panis Sachs MD, Wang TT, Schwartz RE, Lim JK, Albrecht RA, TenOever R. 2020. Imbalanced host response to SARS-CoV-2 drives development of COVID-19. Cell 181:1036–1045.e9. https://doi.org/10.1016/j.cell.2020.04.026.

20. Shannon A, Le NT-T, Selisko B, Eydoux C, Alvarez K, Guillemot J-C, Decroly E, Peersen O, Ferron F, Canard B. 2020. Remdesivir and SARS-CoV-2: structural requirements at both nsp12 RdRp and nsp14 exonuclease active-sites. Antiviral Res 178:104793. https://doi.org/10.1016/j.antiviral.2020.104793.

21. Rambaut A, Holmes EC, O'Toole Á, Hill V, McCrone JT, Ruis C, Du Plessis L, Pybus OG. 2020. A dynamic nomenclature proposal for SARS-CoV-2 lineages to assist genomic epidemiology. Nat Microbiol 5:1403–1407. https://doi.org/10.1038/s41564-020-0770-5.

22. Gonzalez-Reiche AS, Hernandez MM, Sullivan MJ, Ciferri B, Alshammary H, Obla A, Fabre S, Kleiner G, Polanco J, Khan Z, Alburquerque B, van de Guchte A, Dutta J, Francoeur N, Melo BS, Oussenko I, Deikus G, Soto J, Sridhar SH, Wang Y-C, Twyman K, Kasarskis A, Altman Dr Smith M, Sebra R, Aberg J, Krammer F, García-Sastre A, Luksza M, Patel G, Paniz-Mondolfi A, Gitman M, Sordillo EM, Simon V, van Bakel H. 2020. Introductions and early spread of SARS-CoV-2 in the New York City area. Science 369:297–301.

23. Plante JA, Liu Y, Liu J, Xia H, Johnson BA, Lokugamage KG, Zhang X, Muruato AE, Zou J, Fontes-Garfias CR, Mirchandani D, Scharton D, Bilello JP, Ku Z, An Z, Kalveram B, Freiberg AN, Menachery VD, Xie X, Plante KS, Weaver SC, Shi PY. 2020. Spike mutation D614G alters SARS-CoV-2 fitness. Nature https://doi.org/10.1038/s41586-020-2895-3.

24. Hou YJ, Chiba S, Halfmann P, Ehre C, Kuroda M, Dinnon KH, Leist SR, Schäfer A, Nakajima N, Takahashi K, Lee RE, Mascenik TM, Graham R, Edwards CE, Tse LV, Okuda K, Markmann AJ, Bartelt L, de Silva A, Margolis DM, Boucher RC, Randell SH, Suzuki T, Gralinski LE, Kawaoka Y, Baric RS. 2020. SARS-CoV-2 D614G variant exhibits efficient replication ex vivo and transmission *in vivo*. Science 370:1464–1468. https://doi.org/10.1126/science.abe8499.

25. Thornburg N, Bradford R, Rashid S, Flores B, Parker M, Tallon L, Sadzewicz L, Ott S, Vavikolanu K, Nadendla S, Sichtig H. 2020. Data from "FDA Database for Regulatory Grade Microbial Sequences (FDA-ARGOS): supporting development and validation of infectious disease Dx tests."

26. Roder A, Banakis S, Johnson K, Khalfan M, Borenstein E, Samanovic M, Cornelius A, Herati R, Ulrich R, Fleming A, Kottkamp A, Raabe V, Mulligan MJ, Gresham D, Ghedin E. 2020. Data from "SARS-CoV-2 sequences from COVID19 patients in New York." GenBank https://www.ncbi.nlm.nih.gov/nuccore/MT703677.1 (accession no. MT703677.1).

27. Lavi E, Wang Q, Weiss SR, Gonatas NK. 1996. Syncytia formation induced by coronavirus infection is associated with fragmentation and rearrangement of the Golgi apparatus. Virology 221:325–334. https://doi.org/10.1006/viro.1996.0382.

28. Corver J, Broer R, Van Kasteren P, Spaan W. 2009. Mutagenesis of the transmembrane domain of the SARS coronavirus spike glycoprotein: refinement of the requirements for SARS coronavirus cell entry. Virol J 6:230–213. https://doi.org/10.1186/1743-422X-6-230.

29. Kim Y, Lovell S, Tiew K-C, Mandadapu SR, Alliston KR, Battaile KP, Groutas WC, Chang K-O. 2012. Broad-spectrum antivirals against 3C or 3C-like proteases of picornaviruses, noroviruses, and coronaviruses. J Virol 86:11754–11762. https://doi.org/10.1128/JVI.01348-12.

30. Vuong W, Khan MB, Fischer C, Arutyunova E, Lamer T, Shields J, Saffran HA, McKay RT, van Belkum MJ, Joyce MA, Young HS, Tyrrell DL, Vederas JC, Lemieux MJ. 2020. Feline coronavirus drug inhibits the main protease of SARS-CoV-2 and blocks virus replication. Nat Commun 11:4282. https://doi.org/10.1038/s41467-020-18096-2.

31. Gordon CJ, Tchesnokov EP, Woolner E, Perry JK, Feng JY, Porter DP, Götte M. 2020. Remdesivir is a direct-acting antiviral that inhibits RNA-dependent RNA polymerase from severe acute respiratory syndrome coronavirus 2 with high potency. J Biol Chem 295:6785–6797. https://doi.org/10.1074/jbc.RA120.013679.

32. Krichel B, Falke S, Hilgenfeld R, Redecke L, Uetrecht C. 2020. Processing of the SARS-CoV pp1a/ab nsp7–10 region. Biochem J 477:1009–1019. https://doi.org/10.1042/BCJ20200029.

33. Agostini ML, Andres EL, Sims AC, Graham RL, Sheahan TP, Lu X, Smith EC, Case JB, Feng JY, Jordan R, Ray AS, Cihlar T, Siegel D, Mackman RL, Clarke MO, Baric RS, Denison MR. 2018. Coronavirus susceptibility to the antiviral remdesivir (GS-5734) is mediated by the viral polymerase and the proofreading exoribonuclease. mBio 9:e00221-18. https://doi.org/10.1128/mBio.00221-18.

34. Daelemans D, Pauwels R, De Clercq E, Pannecouque C. 2011. A time-of-drug addition approach to target identification of antiviral compounds. Nat Protoc 6:925–933. https://doi.org/10.1038/nprot.2011.330.

35. Reid AT, Sutanto EN, Chander-Veerati P, Looi K, Li NF, Iosifidis T, Loo SL, Garratt LW, Kicic A. 2019. Ground zero—the airway epithelium. In Bartlett N, Wark P, Knight D (ed), Rhinovirus infections: rethinking the impact on human health and disease. Academic Press, London, UK.

36. Dittmann M, Koralov SB, Ruggles K. 2020. Data from "Analysis of 3D human airway epithelial cultures by single-cell RNA-seq." Gene Expression Omnibus https://www.ncbi.nlm.nih.gov/geo/query/acc.cgi?acc=GSE166601 (GEO series GSE166601).

37. Garcíá SR, Deprez M, Lebrigand K, Cavard A, Paquet A, Arguel MJ, Magnone V, Truchi M, Caballero I, Leroy S, Marquette CH, Marcet B, Barbry P, Zaragosi LE. 2019. Novel dynamics of human mucociliary differentiation revealed by single-cell RNA sequencing of nasal epithelial cultures. Development 146:dev177428. https://doi.org/10.1242/dev.177428.

38. Ravindra N, Alfajaro MM, Gasque V, Habet V, Wei J, Filler R, Huston N, Wan H, Szigeti-Buck K, Wang B, Wang G, Montgomery R, Eisenbarth S, Williams A, Pyle AM, Iwasaki A, Horvath T, Foxman E, Pierce R, van Dijk D, Wilen C. 2020. Single-cell longitudinal analysis of SARS-CoV-2 infection in human airway epithelium. bioRxiv https://doi.org/https://doi.org/10.1101/2020.05.06.081695.

39. Greaney AM, Adams TS, Brickman Raredon MS, Gubbins E, Schupp JC, Engler AJ, Ghaedi M, Yuan Y, Kaminski N, Niklason LE. 2020. Platform effects on regeneration by pulmonary basal cells as evaluated by single-cell RNA sequencing. Cell Rep 30:4250–4265.e6. https://doi.org/10.1016/j.celrep.2020.03.004.

40. Suzuyama N, Katoh M, Takeuchi T, Yoshitomi S, Higuchi T, Asashi S, Yokoi T. 2007. Species differences of inhibitory effects on P-glycoprotein-mediated drug transport. J Pharm Sci 96:1609–1618. https://doi.org/10.1002/jps.20787.

41. Walters MS, Gomi K, Ashbridge B, Moore MA, Arbelaez V, Heldrich J, Ding BS, Rafii S, Staudt MR, Crystal RG. 2013. Generation of a human airway epithelium derived basal cell line with multipotent differentiation capacity. Respir Res 14:135. https://doi.org/10.1186/1465-9921-14-135.

42. Liao M, Liu Y, Yuan J, Wen Y, Xu G, Zhao J, Cheng L, Li J, Wang X, Wang F, Liu L, Amit I, Zhang S, Zhang Z. 2020. Single-cell landscape of bronchoalveolar immune cells in patients with COVID-19. Nat Med 26:842–844. https://doi.org/10.1038/s41591-020-0901-9.

43. Liao M, Liu Y, Yuan J, Wen Y, Xu G, Zhao J, Cheng L, Li J, Wang X, Wang F, Liu L, Amit I, Zhang S, Zhang Z. 2020. Data from "Single-cell landscape of bronchoalveolar immune cells in COVID-19 patients." Gene Expression Omnibus https://www.ncbi.nlm.nih.gov/geo/query/acc.cgi?acc=GSE145926 (series GSE145926).

44. Hui KPY, Cheung MC, Perera RAPM, Ng KC, Bui CHT, Ho JCW, Ng MMT, Kuok DIT, Shih KC, Tsao SW, Poon LLM, Peiris M, Nicholls JM, Chan MCW. 2020. Tropism, replication competence, and innate immune responses of the coronavirus SARS-CoV-2 in human respiratory tract and conjunctiva: an analysis in ex-vivo and in-vitro cultures. Lancet Respir Med 8:687–695. https://doi.org/10.1016/S2213-2600(20)30193-4.

45. Chu H, Chan JF-W, Yuen TT-T, Shuai H, Yuan S, Wang Y, Hu B, Yip CC-Y, Tsang JO-L, Huang X, Chai Y, Yang D, Hou Y, Chik KK-H, Zhang X, Fung AY-F, Tsoi H-W, Cai J-P, Chan W-M, Ip JD, Chu AW-H, Zhou J, Lung DC, Kok K-H, To KK-W, Tsang OT-Y, Chan K-H, Yuen K-Y. 2020. Comparative tropism, replication kinetics, and cell damage profiling of SARS-CoV-2 and SARS-CoV with implications for clinical manifestations, transmissibility, and laboratory studies of COVID-19: an observational study. Lancet Microbe 1:e14–e23. https://doi.org/10.1016/S2666-5247(20)30004-5.

46. Sheahan TP, Sims AC, Zhou S, Graham RL, Pruijssers AJ, Agostini ML, Leist SR, Schäfer A, Dinnon KH, Stevens LJ, Chappell JD, Lu X, Hughes TM, George AS, Hill CS, Montgomery SA, Brown AJ, Bluemling GR, Natchus MG, Saindane M, Kolykhalov AA, Painter G, Harcourt J, Tamin A, Thornburg NJ, Swanstrom R, Denison MR, Baric RS. 2020. An orally bioavailable broad-spectrum antiviral inhibits SARS-CoV-2 in human airway epithelial cell cultures and multiple coronaviruses in mice. Sci Transl Med 12:eabb5883. https://doi.org/10.1126/scitranslmed.abb5883.

47. Cao B, Wang Y, Wen D, Liu W, Wang J, Fan G, Ruan L, Song B, Cai Y, Wei M, Li X, Xia J, Chen N, Xiang J, Yu T, Bai T, Xie X, Zhang L, Li C, Yuan Y, Chen H, Li H, Huang H, Tu S, Gong F, Liu Y, Wei Y, Dong C, Zhou F, Gu X, Xu J, Liu Z, Zhang Y, Li H, Shang L, Wang K, Li K, Zhou X, Dong X, Qu Z, Lu S, Hu X, Ruan S, Luo S, Wu J, Peng L, Cheng F, Pan L, Zou J, Jia C, et al. 2020. A trial of lopinavir-ritonavir in adults hospitalized with severe Covid-19. N Engl J Med 382:1787–1799. https://doi.org/10.1056/NEJMoa2001282.

48. Deng X, StJohn SE, Osswald HL, O'Brien A, Banach BS, Sleeman K, Ghosh AK, Mesecar AD, Baker SC. 2014. Coronaviruses resistant to a 3C-like protease inhibitor are attenuated for replication and pathogenesis, revealing a low genetic barrier but high fitness cost of resistance. J Virol 88:11886–11898. https://doi.org/10.1128/jvi.01528-14.

49. Günthard HF, Calvez V, Paredes R, Pillay D, Shafer RW, Wensing AM, Jacobsen DM, Richman DD. 2019. Human immunodeficiency virus drug resistance: 2018 recommendations of the International Antiviral Society–USA panel. Clin Infect Dis 320:379–396. https://doi.org/10.1093/cid/ciy463.

50. Su TH, Liu CJ. 2017. Combination therapy for chronic hepatitis B: current updates and perspectives. Gut Liver 11:590–603. https://doi.org/10.5009/gnl16215.

51. Whitley RJ, Monto AS. 2019. Resistance of influenza virus to antiviral medications. Clin Infect Dis 71:1092–1094. https://doi.org/10.1093/cid/ciz911.

52. Kumar A. 2011. Early versus late oseltamivir treatment in severely ill patients with 2009 pandemic influenza A (H1N1): speed is life. J Antimicrob Chemother 66:959–963. https://doi.org/10.1093/jac/dkr090.

53. Wölfel R, Corman VM, Guggemos W, Seilmaier M, Zange S, Müller MA, Niemeyer D, Jones TC, Vollmar P, Rothe C, Hoelscher M, Bleicker T, Brünink S, Schneider J, Ehmann R, Zwirglmaier K, Drosten C, Wendtner C. 2020. Virological assessment of hospitalized patients with COVID-2019. Nature 581:465–469. https://doi.org/10.1038/s41586-020-2196-x.

54. Jonathan G, Norio O, Daniel S, George D, Erika A, Antonella C, Torsten F, Gary G, Green ML, François-Xavier L, Emanuele N, Rentaro O. 2020. Compassionate use of remdesivir for patients with severe Covid-19. N Engl J Med 382:2327–2336. https://doi.org/10.1056/NEJMoa2007016.

55. Chaudhary PM, Mechetner EB, Roninson IB. 1992. Expression and activity of the multidrug resistance P-glycoprotein in human peripheral blood lymphocytes. Blood 80:2735–2739. https://doi.org/10.1182/blood.V80.11.2735.2735.

56. Egashira M, Kawamata N, Sugimoto K, Kaneko T, Oshimi K. 1999. P-glycoprotein expression on normal and abnormally expanded natural killer cells and inhibition of P-glycoprotein function by cyclosporin A and its analogue, PSC833. Blood 93:599–606. https://doi.org/10.1182/blood.V93.2.599.402k06_599_606.

57. Chen ML, Sun A, Cao W, Eliason A, Mendez KM, Getzler AJ, Tsuda S, Diao H, Mukori C, Bruno NE, Kim SY, Pipkin ME, Koralov SB, Sundrud MS. 2020. Physiological expression and function of the MDR1 transporter in

cytotoxic T lymphocytes. J Exp Med 217:e20191388. https://doi.org/10
.1084/jem.20191388.

58. Cao W, Kayama H, Chen ML, Delmas A, Sun A, Kim SY, Rangarajan ES, McKevitt K, Beck AP, Jackson CB, Crynen G, Oikonomopoulos A, Lacey PN, Martinez GJ, Izard T, Lorenz RG, Rodriguez-Palacios A, Cominelli F, Abreu MT, Hommes DW, Koralov SB, Takeda K, Sundrud MS. 2017. The xenobiotic transporter Mdr1 enforces T cell homeostasis in the presence of intestinal bile acids. Immunity 47:1182–1196.e10. https://doi.org/10.1016/j .immuni.2017.11.012.

59. Fung KL, Pan J, Ohnuma S, Lund PE, Pixley JN, Kimchi-Sarfaty C, Ambudkar SV, Gottesman MM. 2014. MDR1 synonymous polymorphisms alter transporter specificity and protein stability in a stable epithelial monolayer. Cancer Res 74:598–608. https://doi.org/10.1158/0008-5472.CAN-13-2064.

60. Gralinski LE, Menachery VD. 2020. Return of the coronavirus: 2019-nCoV. Viruses 12:135–138. https://doi.org/10.3390/v12020135.

61. Volz E, Mishra S, Chand M, Barrett JC, Johnson R, Hopkins S, Gandy A, Rambaut A, Ferguson NM. 2021. Transmission of SARS-CoV-2 Lineage B.1.1.7 in England: insights from linking epidemiological and genetic data. medRxiv https://doi.org/https://doi.org/10.1101/2020.12.30.20249034.

62. Tegally H, Wilkinson E, Lessells RR, Giandhari J, Pillay S, Msomi N, Mlisana K, Bhiman J, Allam M, Ismail A, Engelbrecht S, van Zyl G, Preiser W, Williamson C, Pettruccione F, Sigal A, Gazy I, Hardie D, Hsiao M, Martin D, York D, Goedhals D, San EJ, Giovanetti M, Lourenco J, Alcantara LC, de Oliveira T. 2020. Major new lineages of SARS-CoV-2 emerge and spread in South Africa during lockdown. medRxiv https://doi.org/https://doi.org/10 .1101/2020.10.28.20221143.

63. Faria N, Claro IM, Candido D, Franco LAM, Andrade PS, Coletti TM, Silva CAM, Sales FC, Manuli ER, Aguiar RS, Gaburo N, Camilo CDC, Fraiji NA, Crispim MAE, Carvalho MDPSS, Rambaut A, Loman N, Pybus OG, Sabino EC, the CADDE Genomic Network. 12 Jan 2021. Genomic characterisation of an emergent SARS-CoV-2 lineage in Manaus: preliminary findings. Virological.org.

64. Seifert LL, Si C, Saha D, Sadic M, De Vries M, Ballentine S, Briley A, Wang G, Valero-Jimenez AM, Mohamed A, Schaefer U, Moulton HM, García-Sastre A, Tripathi S, Rosenberg BR, Dittmann M. 2019. The ETS transcription factor ELF1 regulates a broadly antiviral program distinct from the type i interferon response. PLoS Pathog 15:e1007634. https://doi.org/10.1371/ journal.ppat.1007634.

65. Johnson BA, Xie X, Bailey AL, Kalveram B, Lokugamage KG, Muruato A, Zou J, Zhang X, Juelich T, Smith JK, Zhang L, Bopp N, Schindewolf C, Vu M, Vanderheiden A, Winkler ES, Swetnam D, Plante JA, Aguilar P, Plante KS, Popov V, Lee B, Weaver SC, Suthar MS, Routh AL, Ren P, Ku Z, An Z, Debbink K, Diamond MS, Shi PY, Freiberg AN, Menachery VD. 2021. Loss of furin cleavage site attenuates SARS-CoV-2 pathogenesis. Nature https://doi.org/10 .1038/s41586-021-03237-4.

66. Mimitou EP, Cheng A, Montalbano A, Hao S, Stoeckius M, Legut M, Roush T, Herrera A, Papalexi E, Ouyang Z, Satija R, Sanjana NE, Koralov SB, Smibert P. 2019. Multiplexed detection of proteins, transcriptomes, clonotypes and CRISPR perturbations in single cells. Nat Methods 16:409–412. https://doi.org/10.1038/s41592-019-0392-0.

67. Stoeckius M, Zheng S, Houck-Loomis B, Hao S, Yeung BZ, Mauck WM, Smibert P, Satija R. 2018. Cell hashing with barcoded antibodies enables multiplexing and doublet detection for single cell genomics. Genome Biol 19:224. https://doi.org/10.1186/s13059-018-1603-1.

68. Stuart T, Butler A, Hoffman P, Hafemeister C, Papalexi E, Mauck WM, Hao Y, Stoeckius M, Smibert P, Satija R. 2019. Comprehensive integration of singlecell data. Cell 177:1888–1902.e21. https://doi.org/10.1016/j.cell.2019.05.031.